Open access • Journal Article • DOI:10.1038/NMAT4579

Controlled lateral anisotropy in correlated manganite heterostructures by interface-engineered oxygen octahedral coupling — Source link

Zhaoliang Liao, Mark Huijben, Zhicheng Zhong, Nicolas Gauquelin ...+11 more authors

Institutions: MESA+ Institute for Nanotechnology, Vienna University of Technology, University of Antwerp, University of British Columbia ...+1 more institutions

Published on: 01 Apr 2016 - Nature Materials (Nature Publishing Group)

Topics: Magnetic anisotropy, Magnetization, Manganite and Ferromagnetism

Controlled lateral anisotropy in correlated manganite heterostructures by interface-engineered oxygen octahedral coupling

Reference:

Liao Z., Huijben M., Zhong Z., Gauquelin Nicolas, Van Aert Sandra, Verbeeck Johan, Van Tendeloo Gustaaf, et al..- Controlled lateral anisotropy in correlated manganite heterostructures by interface-engineered oxygen octahedral coupling
Nature materials - ISSN 1476-1122 - 15:4(2016), p. 425-431
Full text (Publishers DOI): http://dx.doi.org/doi:10.1038/NMAT4579
To cite this reference: http://hdl.handle.net/10067/1331900151162165141

Controlled lateral anisotropy in correlated manganite heterostructures by interface-engineered oxygen octahedral coupling

Z. Liao[1], M. Huijben[1*], Z. Zhong[2], N. Gauquelin[3], S. Macke[4,5], R. J. Green[4,6], S. Van Aert[3], J. Verbeeck[3], G. Van Tendeloo[3], K. Held[2], G. A. Sawatzky[4], G. Koster[1] & G. Rijnders[1]

[1]*MESA*$^+$ *Institute for Nanotechnology, University of Twente, P.O.BOX 217, 7500 AE, Enschede, The Netherlands*

[2]*Institute of Solid State Physics, Vienna University of Technology, A-1040 Vienna, Austria*

[3]*Electron Microscopy for Materials Science (EMAT), University of Antwerp, 2020 Antwerp, Belgium*

[4]*Quantum Matter Institute and Department of Physics and Astronomy, University of British Columbia, 2355 East Mall, Vancouver, V6T 1Z4, Canada*

[5]*Max Planck Institute for Solid State Research, Heisenbergstraße 1, 70569 Stuttgart, Germany*

[6]*Max Planck Institute for Chemical Physics of Solids, Nöthnitzerstraße 40, 01187 Dresden, Germany*

Controlled in-plane rotation of the magnetic easy axis in manganite heterostructures by tailoring the interface oxygen network could allow the development of correlated oxide-based magnetic tunneling junctions with non-collinear magnetization, with possible practical applications as miniaturized high-switching-speed magnetic random access memory (MRAM) devices[1,2]. Here, we demonstrate how to manipulate magnetic and electronic anisotropic properties in manganite heterostructures by engineering the oxygen network on the unit-cell level. The

---

[*] email: m.huijben@utwente.nl

strong oxygen octahedral coupling is found to transfer the octahedral rotation, present in the $NdGaO_3$ (NGO) substrate, to the $La_{2/3}Sr_{1/3}MnO_3$ (LSMO) film in the interface region. This causes an unexpected realignment of the magnetic easy axis along the short axis of the LSMO unit cell as well as the presence of a giant anisotropic transport in these ultrathin LSMO films. As a result we possess control of the lateral magnetic and electronic anisotropies by atomic scale design of the oxygen octahedral rotation.

Emergent phenomena in oxide heterostructures[3,4] such as interface charge transfer[5], two dimensional free electron gas[6] and ferromagnetism between two non-magnetic materials[7], are induced by the dedicated coupling between spin, orbital, charge and lattice degrees of freedom[8,9]. Developing strategies to engineer these intimate couplings in oxide heterostructures is crucial to achieve new phenomena and to pave the path towards novel functionalities with atomic scale dimensions. Utilizing polar discontinuity[6], inducing strain[10-12], charge transfer[5], and spatial confinement[13,14] are several well-known strategies. In ABO_3 perovskites orbital, charge and spin order are intimately correlated to the BO_6 oxygen octahedra[15-22]. In the bulk, the oxygen octahedral rotation (OOR) and deformation are usually controlled by isovalent substitution or by the deployment of high pressure[15-21], but oxide heterostructures offer additional ways to tune the lattice structure[3,4,12,22-26]. The OOR can be tailored either by strain or interfacial oxygen octahedral coupling (OOC)[25-29]. The OOC is a geometric constraint effect which forces the octahedra in a film to rotate due to a retained corner-connectivity of oxygen octahedra across an interface[25].

For decades, strain has been used for heterostructure engineering, but strain is usually a long range effect depending on lattice mismatch[30] and therefore less controllable at the atomic scale, limiting its application towards complex devices where films with varying local properties on a single wafer are required. The OOC, which unlike strain has a short impact length scale of ~ 2 nm[25-29], could be a new route to realize atomic scale control of material properties and functionalities. However, the questions are still open whether the OOC can compete with strain, how strong of an impact it can make on the functionalities and if it can transfer not only the magnitude of rotation but also the Glazer rotation pattern[31] to a film. Such controllable OOR will provide a feasible new route to the artificial design of structures with novel functionalities.

By utilizing the OOC at the LSMO and NGO (110) interface, we demonstrate the possibility to transfer the characteristic NGO anisotropic structure into epitaxial LSMO films. This in turn creates not only new but also switchable magnetic and electronic anisotropies. The rhombohedral LSMO possesses an $a^-a^-a^-$ rotation which results in an isotropic B-O-B bond angle (θ) and isotropic properties[18]. The Glazer symbol[31] here and after is sequentially corresponding to the rotation along *a*, *b* and *c* axis respectively. In contrast, the orthorhombic NGO possesses an $c^+a^-a^-$ rotation with a larger θ along the [001] direction than along the [1-10] direction[32]. For convenience, pseudo-cubic indices are used for NGO with *a*, *b* and *c* corresponding to [001], [1-10] and [110] respectively. The structural characteristics of LSMO and NGO give rise to in-phase vs. out–of-phase rotation type mismatch occurring along the *a*-axis (see left panel of Fig. 1a) while both are out-of-phase along the *b*-axis (see right panel of Fig. 1a). The magnitude of the bond angle θ also has a certain degree of mismatch: ~154 ° in NGO vs. 166.3 ° in LSMO. As a result, both the anisotropic rotation type mismatch and the large difference (~12^{o}) in bond angle will cause a strong discontinuity of the octahedra (see Fig. 1a). Therefore, the oxygen atoms need to rearrange at the interface, resulting in a large change of the OOR in the LSMO film.

The effect of the OOC at the LSMO/NGO interface is visualized by atomically resolved Cs-corrected scanning transmission electron microscopy (STEM). Thin LSMO films have been grown by pulsed laser deposition on NGO (110) substrates[33] (see method and Supplementary Fig. S1). All films are fully strained to NGO (See Supplementary Fig. S2), resulting an overall ~ 0.4% compressive strain on LSMO with 0.2% in-plane anisotropy[18,32]. Atomic ordering and chemically sharp interfaces were achieved for the samples investigated in this article as demonstrated by the atomic electron energy loss spectroscopy (EELS) maps (See Supplementary Fig. S3). The in-phase rotation along *a*-axis enables us to directly visualize and quantify the BO_6 octahedral tilt in *bc* plane through the Annular Bright-Field STEM (ABF-STEM) image (see Fig.1b)[29,34]. The LSMO strongly follows the NGO rotation characteristic and becomes in-phase along the *a*-axis, which in bulk LSMO is out-of-phase. Close to the interface, the MnO_6 octahedral tilt angle is comparable to that of GaO_6, as shown by the depth profile of BO_6 tilt angle across the interface in Fig. 1e (For estimation of tilt angle, see Supplementary Fig. S4). The tilt angle continuously changes from the GaO_6 substrate value to bulk MnO_6 (far from interface). Interestingly, the first 2 uc layers of LSMO have almost the same tilt angle as NGO. The impact of the octahedral coupling decays rapidly away from the interface and disappears above 4 uc layers. Therefore, the OOC at the LSMO/NGO interface results in the alteration of the OOR (in-phase, out-of-phase) of the LSMO close to the interface, in which the magnitude of the tilt angle is comparable to that of NGO (Fig. 1b). Because of the short impact length scale of OOC, the OOR of the LSMO can be significantly altered by inserting a non-tilted $SrTiO_3$ (STO) buffer layer (Fig. 1c). Within the STO layer, the OOR is also coupled to the OOR of NGO, but the tilt angle relaxes quickly, i.e., the tilt of TiO_6 octahedra starts to disappear above 2 uc layers. Consequently, the LSMO connects to a non-tilted OOR and doesn't show any evidence, within the STEM spatial resolution, of tilting of the MnO_6 octahedra from the first layer (see Fig. 1e). Due to steep decay of tilt in STO, 1 uc STO buffer layer is found to be thick enough to significantly reduce the tilt in LSMO (see Fig. 1d-e). Together with non-buffered LSMO, the resulting interface structure of LSMO indicates that the local OOR at the substrate surface acts as a controllable template for the structure of the epitaxial LSMO film.

The observed interfacial OOC has a dramatic impact on the magnetic properties. The 9 uc STO buffer layer reduces the octahedral tilt in LSMO, thus enhances the magnetism, i.e., 9 uc STO buffer layer increases the Curie temperature (T_C) of the 6 uc LSMO from 145 K to 240 K. The enhancement is already found when using a 1 uc STO buffer layer as the 6 uc LSMO film exhibits a T_C of 180 K, consistent with the observed reduced tilt in LSMO by 1 uc STO buffer layer (see Fig. 1d). The saturated magnetic moment of such STO-buffered LSMO is also larger than the non-buffered LSMO film (see Fig. 2a-c).

Beyond the enhancement, a more striking phenomenon is the switch of magnetic anisotropy (MA) by engineering the interfacial OOR. Due to the different OOR pattern, the 6 uc thick LSMO films with or without STO buffer layer have a different magnetization easy axis, although both exhibit uniaxial MA. The easy axis of the non-buffered LSMO is the *a*-axis as shown in Fig. 2a, in strong contrast to the observed *b*-axis easy axis in thick LSMO films[33,35]. When inserting a STO buffer layer with a thickness ranging from 1 uc to 36 uc (LSMO/STO/NGO) the easy axis is again switched to the *b*-axis. The magnetic behavior of 6 uc LSMO films on top of a 1 uc STO and 9 uc STO buffer layer is shown as example in respectively Figures 2b and 2c. For convenience, the MA with easy axis along the short axis *a* is defined as interfacial MA (IMA) while an easy axis along the long axis *b* is indicated as bulk MA (BMA). Comparison between the structure of LSMO with and without STO buffer layer indicates that the IMA is correlated to the strong tilted LSMO structure while the BMA comes from the nearly non-tilted (NNT) structure. A single unit cell STO buffer layer is thick enough to reduce the tilt in LSMO and thus to switch the easy axis of LSMO (see Fig. 1d and Fig. 2b), indicating the capability to tune the anisotropic properties by atomic scale control. By separating IMA and BMA with a STO barrier in LSMO/STO/LSMO/NGO magnetic tunneling junctions, we are now able to realize orthogonal magnetization between top and bottom LSMO electrodes (See Supplementary Fig. S5). Furthermore, patterning of the STO buffer layer allows us now also to artificially create in-plane magnetic domains (See Supplementary Fig. S5).

The depth profiles of the magnetization further confirm that IMA arises from the strongly tilted interface structure. The atomic concentration profile and magnetic depth profile in 6 uc LSMO films with and without the STO buffer layer have been probed by resonant X-ray reflectometry (RXR)[36] as shown in Fig. 2d (For details of the RXR experiment, see Supplementary Fig. S6). A depth profile of Mn magnetization (M) can be obtained from the best fit of the asymmetric spectra between left and right circular polarized light. The profiles of Ga, Ti and Mn atomic concentration are shown as well for comparison and indicate an atomic sharp interface with negligible interfacial intermixing. The active magnetic layers in these two samples are all located at the interface region. Our magnetic profiles also reveal the presence of magnetic dead layers near the surface[37] for both buffered and non-buffered LSMO films. The OOC has an impact length scale of ~2 nm and, therefore, could have an influence on the surface part of our ultrathin LSMO films on NGO, which can be excluded for our thicker LSMO films. A more detailed analysis will be performed in a future study. Compared with the non-buffered LSMO, the less distorted buffered LSMO film exhibited a more uniform magnetism due to the reduced structural distortion at the interface as well as a reduced thickness of the dead layer on the surface. This fact could explain the observed enhanced saturated magnetization in buffered LSMO film as shown in Fig. 2a-c. Interestingly, the active magnetic layer in the non-buffered LSMO is the ~3 uc interface region and thus coincident with the strong tilted layer (See bottom panel of Fig. 2d). Therefore, the IMA is correlated to the strong tilted LSMO structure while the BMA is coupled to NNT structure.

The distinct OOR patterns near and far from the interface region, give rise to a sharp transition of the MA at 8 uc LSMO layer thickness, see Fig. 3. The contribution from the NNT part to the magnetic anisotropic energy (MAE) will increase with increasing thickness, hence thicker films ($t > 8$ uc) exhibit BMA. The strong tilt part dominates in thinner films with $t < 8$ uc, hence these films exhibit IMA. At 8 uc, the competition between IMA and BMA results in biaxial anisotropy with the easy axis along *ab* and *–ab* directions. The thickness dependence of LSMO thin films further indicates that IMA arises from an interfacial NGO-like OOR pattern, while the strain-dominated NNT part gives rise to BMA.

Concomitant with the MA, the electronic transport properties in the LSMO films are found to exhibit anisotropies as well with a sharp transition at a thickness of 8 uc. Besides a thickness dependent metal insulator transition[38] also an interfacial OOC driven giant transport anisotropy is observed in LSMO films with thicknesses of 6 and 7 uc, which exhibit higher electrical conductivities along the *a*-axis, see Fig. 4a. In thicker films where OOC subsides, the anisotropy becomes much smaller. No thermal hysteresis is observed in the cooling down and warming up cycles, so that a possible anisotropic percolation in a phase separation scenario is excluded[11]. Figure 4b shows the resistivity along two different directions *a* vs *b* at 50 K. Almost 2 orders of magnitude difference of resistivity between the two directions is observed in the 6 uc sample, significantly larger than previously reported strain induced transport anisotropy[39] in LSMO/$DyScO_3$. This difference decreases with increasing thickness, and for t $\geqslant$ 8 uc, this difference is too small to note any anisotropy. However, the temperature dependent magnetoresistance, MR = (R(B)-R(0))/R(0), in Fig. 4c still reflects the presence of transport anisotropy in thick films. Both thin film (6 uc) and thick film (12 uc) exhibit anisotropic MR effect with peak position T_{P}, which reflects a metal-to-insulator transition in manganites (See Supplementary Fig. S7). However, the sign of $\Delta T_P=T_p(a)-T_p(b)$ for 6 uc and 12 uc films are opposite. Therefore, there is a switch of transport anisotropy with increasing thickness. As shown in Fig. 4d, the difference ΔT_P is thickness dependent and becomes zero at 8 uc. For t < 8uc, it is reversed and as large as ΔT_P = 52 K for 6 uc LSMO, whereas in films with t > 8 uc, it is only about – 2 K. Since the more conductive axis has higher T_P and based on Fig. 3 and Fig. 4d, we can conclude that the easy axis for electronic transport (more conductive axis) coincides with the magnetic easy axis of the LSMO films. By switching the magnetic easy axis of a 6 uc LSMO film through introducing a STO buffer layer, the transport easy axis is also switched to the *b*-axis (See Supplementary Fig. S7).

Let us now turn to the mechanism of the thickness driven switch of the anisotropic properties. Since strain does not change with thickness and interfacial intermixing is negligible, the transition of MA with thickness can be expected to correlate with the OOR pattern. Along the *a*-axis, an in-phase (NGO) and out-of-phase (LSMO) mismatch would cause huge oxygen displacements to retain the connectivity of the oxygen octahedra. Furthermore, the rotation of MnO_6 octahedra along the *a*-axis causes the bond angle θ along the *b*-axis to become smaller. While along the *b*-axis, the OOR pattern for both LSMO and NGO are out-of-phase, the displacement of oxygen atoms necessary to match the substrate is less. As a result, the bond angle along the *a*-axis is larger than along the *b*-axis, $\theta(a) > \theta(b)$, which is further evidenced by the STEM images of LSMO/NGO cross-section with zone axis along *b*-axis (see Supplementary Fig. S8 and Fig. S9). Further away from the interface, the OOC effect subsides and the strain dominates, resulting in $\theta(b) > \theta(a)$[40]. Based on the above consideration, a structural evolution of a LSMO film is schematically shown in Fig. 5a. The LSMO film is divided into two regions, the interface OOC driven $b^+a^-c^-$ and the strained induced[40] $a^+b^-c^-$. The larger rotation along *c*-axis for both regions is due to LSMO in-plane compressive strain, which increases the rotation along *c*-axis to give rise to a smaller in-plane lattice constant[40]. In the cross-over thickness the complete LSMO film can be averagely described by $a^+a^-c^-$ and $\langle\theta(a)\rangle \approx \langle\theta(b)\rangle$. The structure characteristic of LSMO near the interface is expected to cause an anisotropic bandwidth (w) according to formula[41] $w \propto \frac{Cos(\pi-\theta)/2}{d^{3.5}}$ with $w(a) > w(b)$. Further away from the interface region, $\theta(b) > \theta(a)$ leads to $w(b) > w(a)$. The expected changes of anisotropic bond angle and bandwidth are consistent with our observed anisotropic transport properties within the double exchange model[42].

According to Fig. 1b, the lattice structure of LSMO films relaxes with thickness and becomes bulk-like at a thickness of about 4 uc. Therefore, in thick LSMO films we expect the presence of two regions: an interface region where the anisotropic properties in each layer change with layer position and a strain dominated bulk region where the anisotropic properties are less dependent on layer position. The uniaxial MAE is described by $E = K_u \text{Cos}^2\varphi$ where φ is an in-plane angle relative to a-axis. For uniaxial anisotropy $K_u = E(a)-E(b)$ is positive or negative, indicating that the easy axis is the b or a-axis, respectively; for biaxial anisotropy $K_u = 0$. The total K_u can be expressed by $K_{tot} = \sum_{n=1}^{t} K_u(n)$, where $K_u(n)$ is MAE constant of the nth layer. The mean MAE constant $<K>$ ($= K_{tot}/t$), (For measurement of <K>, see Supplementary Fig. S10), is found to nonlinearly depend on thickness (see Fig. 5b). The $<K>$ exhibits clear thickness dependence and a cross-over transition from positive to negative values, which can be observed at 8 uc. In contrast, the K_{tot} is linearly dependent on thickness when $t > 8$ uc (see Fig. 5b). Therefore, K_{tot} can be rewritten as $K_{tot} = \sum_{n=1}^{t_I} K_u(n) + K_{uB}(t - t_I) = K_{uB}t - c$. Here, t_I is thickness of interface region beyond which the $K_u(n)$ is approximated to be constant K_{uB} and c is a constant. K_{uB} and c, as obtained from linear fitting of K_{tot} vs. t curve at $t > 8$ uc, are 14.4 μeV/uc and 103.7 μeV/uc, respectively. With these parameters, a critical thickness (t_c), where these sub-layers do not contribute to K_{tot} $(K_{uB}t_c - c = 0)$, can be estimated to be 7.2 uc, in good agreement with the observed 8 uc critical thickness for <K> = 0 as determined by the MA measurements.

To understand the microscopic origin of the MA and the expected coupling between transport and MA, we construct by means of density functional theory (DFT) a tight binding Hamiltonian of LSMO ultrathin films: $\sum_R t_{\alpha\beta}(\vec{R})\, e^{i\vec{K}\cdot\vec{R}} + \left(\frac{\lambda}{2}\right)\sigma(\theta,\varphi) + \xi L \cdot S$ (See Supplementary Fig. S11 and S12). Here, $t_{\alpha\beta}(\vec{R})$ represents the hopping integral from orbital α at site 0 to orbital β at site $\vec{R}$. The structural change due to OOC and strain mainly affects the $t_{\alpha\beta}(\vec{R})$, which in turn leads to a change of the MAE. The hopping terms $t_{\alpha\beta}(\vec{R})$ can be qualitatively indicated by the transport properties in our experiment. We therefore simply mimic the structural and transport anisotropy by introducing anisotropic hopping terms[42] parametrized by A_t: $t_0(\vec{a})$ and $t_0(\vec{b}) = t_0(\vec{a})\,(1 - A_t)$ along $\vec{a}$ and $\vec{b}$ respectively. The calculation of the MAE indicates an in-plane easy axis for a monolayer LSMO film (See Supplementary Fig. S12), while the easy axis in the *ab*-plane depends on the asymmetric hopping factor A_t (see Fig. 5c). In the case of an isotropic in-plane structure (A_t = 0), a biaxial anisotropy with easy axis $[110]_{pc}$ is obtained consistent with observations in (001) LSMO films on cubic STO and $(LaAlO_3)_{0.3}(Sr_2AlTaO_6)_{0.7}$ substrates (see Supplementary Fig. S13). If $t_0(\vec{a})$ is 0.5% percent higher than $t_0(\vec{b})$ (A_t = 0.5%), the easy axis is rotated from the *ab* direction to the *a*-axis and the film becomes uniaxially anisotropic, while A_t = -0.5% will switch the easy axis to the *b*-axis. Thus the easy axis prefers to align along the axis with the largest hopping amplitude, which is also the axis for the largest conductivity as in experiment.

The calculated in-plane anisotropic energy is of the order of 4 μeV/uc, qualitatively consistent with the experimental observations.

In conclusion, OOC driven magnetic and transport anisotropies are realized in LSMO/NGO heterostructures. Competition between the interfacial OOC and the strain further away from the interface leads to a thickness driven sharp transition of the anisotropic properties. The observed coupling of transport and MA as well as the tight-binding modeling indicate the key role of the anisotropic bandwidth for the anisotropic properties in LSMO. Our finding will also provide new insight into the recently reported strain driven transport anisotropy in manganite films[11,39,42]. The observed OOC can be extended into other perovskite oxide heterostructures or superlattices. Furthermore, the revealed competition between OOC and strain which results in thickness dependent properties should have significant impact on the understanding of widely reported reduced dimensionality effect in many correlated perovskite ultrathin films.

Our results unequivocally link the atomic structure near interfaces to macroscopic properties. The strong correlation between controllable oxygen network and functionalities will have significant impact on both fundamental research and technological application of correlated perovskite heterostructures. By controlling interfacial OOC, we are now able to pattern in 3 dimensions the magnetization to achieve non-collinear magnetization in both in-plane and out of plane directions, thus making the heterostructures promising for application in orthogonal spin transfer devices, spin oscillators and low field sensors. Moreover, one could extend the revealed competition between strain and OOC to a new direction to realize piezoelectric control of magnetization reversal for spintronics application by tuning balance between those two co-existent effects.

Note added in proof: After this manuscript was accepted we noticed the work by another group also reporting control of the oxide-interface properties by interface-engineering[47].

Methods

LSMO thin films were grown on atomically flat NGO (110) substrates from a stoichiometric $La_{2/3}Sr_{1/3}MnO_3$ target by pulsed laser deposition using a KrF excimer laser operating at 248 nm. The atomically flat NGO substrate, as confirmed by atomic force microscopy (AFM), was obtained by BHF chemical etching and subsequent annealing at 1050 ^{o}C for 4 hours[33]. The laser fluence and repetition rate were 0.6 J/cm^2 and 2 Hz respectively. The oxygen partial pressure and substrate temperature were maintained at 0.2 mBar and 680 ^{o}C respectively during the growth. The growth process was monitored by reflection high-energy electron diffraction (RHEED), which confirmed the layer by layer characteristic growth.

Scanning transmission electron microscopy (STEM) was performed on the X-Ant-Em instrument at the University of Antwerp. Cross-sectional cuts of the samples along the [1-10] and [001] directions were prepared using a FEI Helios 650 dual-beam Focused Ion Beam device. The 6 uc LSMO film was capped with a 10 nm STO layer grown at room temperature in order to prevent LSMO ultrathin layer from damage during the preparation of TEM cross-section specimen in both buffered and un-buffered cases. Satisfactory samples were prepared using very low energy ion beam thinning subsequent to a protection of the sample surface by sputtering of a 10 nm thick carbon protection layer, followed be E-beam deposition of Platinum as a first step to the FIB lamella preparation procedure. The Electron Microscope used consists of an FEI Titan G3 electron microscope equipped with an aberration corrector for the probe-forming lens as well as a high-brightness gun and a Super-EDX 4-quadrant detector operated at 300 kV acceleration voltage for the EDX experiments and STEM-ADF and ABF imaging. The

STEM convergence semi-angle used was 21 mrad, providing a probe size of ~0.8 Å. The collection semi-angle ranges from 11-29 mrad and 29-160 mrad for ABF and ADF imaging respectively.

Magnetic and transport properties were measured by using a Quantum Design Vibration Sample Magnetometer (VSM) and a Physical Properties Measurement System (PPMS) respectively. The magnetization of the LSMO films was acquired by subtracting the paramagnetic signal of each NGO substrate (See Supplementary Fig. S14). The transport properties were analyzed in a van-der-Pauw geometry, in which the resistances along *a* and *b*-axis were measured simultaneously.

The magneto-optical profile was measured using x-ray resonant magnetic reflectivity (XRMR)[43]. The XRMR experiments were performed using an in-vacuum 4-circle diffractometer at the Resonant Elastic and Inelastic X-ray Scattering (REIXS) beamline of the Canadian Light Source (CLS) in Saskatoon, Canada[44]. The beamline has a flux of 5×10^{12} photon/s and photon energy resolution $\Delta E/E$ of ~ 10^{-4}. The base pressure of the diffractometer chamber was kept lower than 10^{-9} Torr. The samples were aligned with their surface normal in the scattering plane and measured at a temperature of 20 K. The measurements were carried out in the specular reflection geometry with several nonresonant photon energies as well as energies at the Mn $L_{2,3}$ resonance (~635-660 eV). For details about the magneto-optical profile extraction, see Supplementary Fig. S6.

A DFT based tight binding Hamiltonian was constructed to calculate the MAE of LSMO ultrathin films, $H(\vec{k}) + \left(\frac{\lambda}{2}\right)\sigma(\theta,\varphi) + \xi L \cdot S$, including exchange splitting λ and spin-orbit coupling ξ. The first term $H(\vec{k})$, paramagnetic tight binding Hamiltonian, is constructed on Wannier basis projected from DFT calculated Bloch waves of LSMO near Fermi level. The Wannier projection was performed with Wien2Wannier package, employing Wannier90 for constructing maximally localized Wannier orbitals[45]. The second term $\left(\frac{\lambda}{2}\right)\sigma(\theta,\varphi)$ leads to an exchange splitting λ for spins parallel and antiparallel to (θ, φ) direction. We set $\lambda = 2$eV which is the typical exchange splitting in manganites[46]. The last term is the atomic spin orbit coupling of Mn *d* orbitals with $\xi = 0.05$ eV. A very fine k mesh (e.g. 160 × 160 × 160) was used to make sure that the total energy converges down to 10^{-3} μeV accuracy.

References:

[1] Brataas, A., Kent, A.D. & Ohno, H., Current-induced torques in magnetic materials, *Nature Mater.* **11**, 372 (2012).

[2] Brataasa, A., Bauer, G.E.W. & Kelly, P.J., Non-collinear magnetoelectronics, *Phys. Rep.* **427**, 157 (2006).

[3] Hwang, H.Y., Iwasa, Y., Kawasaki, M., Keimer, B., Nagaosa, N. & Tokura, Y., Emergent phenomena at oxide interfaces, *Nature Mater.* **11**, 103 (2012).

[4] Zubko, P., Gariglio, S., Gabay, M., Ghosez, P. & Triscone, J.-M., Interface Physics in Complex Oxide Heterostructures, *Annu. Rev. Condens. Matter Phys.* **2**, 141 (2011).

[5] Chakhalian, J., Freeland, J.W., Habermeier, H.-U., Cristiani, G., Khaliullin, G., van Veenendaal, M. & Keimer, B., Orbital reconstruction and covalent bonding at an oxide interface, *Science* **318**, 1114–1117 (2007).

[6] Ohtomo, A. & Hwang, H.Y., A high-mobility electron gas at the $LaAlO_3/SrTiO_3$ heterointerface, *Nature* **427**, 423 (2004).

[7] Brinkman, A., Huijben, M., van Zalk, M., Huijben, J., Zeitler, U., Maan, J.C., van der Wiel, W.G., Rijnders, G., Blank, D.H.A. & Hilgenkamp, H., Magnetic effects at the interface between non-magnetic oxides, *Nature Mater.* **6**, 493 (2007).

[8] Tokura, Y. & Nagaosa, N., Orbital physics in transition-metal oxides, *Science* **288**, 462 (2000).

[9] Dagotto, E., Complexity in strongly correlated electronic systems, *Science* **309**, 257 (2005).

[10] Aetukuri, N.B., Gray, A.X., Drouard, M., Cossale, M., Gao, L., Reid, A.H., Kukreja, R., Ohldag, H., Jenkins, C.A., Arenholz, E., Roche, K.P., Dürr, H.A., Samant, M.G. & Parkin, S.P., Control of the metal–insulator transition in vanadium dioxide by modifying orbital occupancy, Nature Phys. 9, 661 (2013).

[11] Ward, T.Z., Budai, J.D., Gai, Z., Tischler, J.Z., Yin, L. & Shen, J., Elastically driven anisotropic percolation in electronic phase-separated manganites, *Nature Phys.* **5**, 885 (2009).

[12] Schlom, D.G., Chen, L.-Q., Eom, C.-B., Rabe, K.M., Streiffer, S.K. & Triscone, J.-M., Strain tuning of ferroelectric thin films, *Ann. Rev. Mater. Res.* **37**, 589 (2007).

[13] Boris, A.V., Matiks, Y., Benckiser, E., Frano, A., Popovich, P., Hinkov, V., Wochner, P., Castro-Colin, M., Detemple, E., Malik, V.K., Bernhard, C., Prokscha, T., Suter, A., Salman, Z., Morenzoni, E., Cristiani, G., Habermeier, H.-U. & Keimer, B., Dimensionality control of electronic phase transitions in nickel-oxide superlattices, *Science* **332**, 937 (2011).

[14] King, P.D.C, Wei, H.I., Nie, Y.F., Uchida, M., Adamo, C., Zhu, S., He, X., Božović, I., Schlom, D.G. & Shen, K.M., Atomic-scale control of competing electronic phases in ultrathin $LaNiO_3$, *Nat. NanoTech.* **9**, 443 (2014).

[15] Salamon, M.B. & Jaime, M., The physics of manganites: Structure and transport, *Rev. Mod. Phys.* **73**, 583 (2001).

[16] Coey, J.M.D., Viret, M. & von Molnaír, S., Mixed-valence manganites, *Adv. Phys.* **48**, 167 (1999).

[17] Chmaissem, O., Dabrowski, B., Kolesnik, S., Mais, J., Brown, D.E., Kruk, R., Prior, P., Pyles, B. & Jorgensen, J.D., Relationship between structural parameters and the Néel temperature in $Sr_{1-x}Ca_xMnO_3$ (0<~x<~1) and $Sr_{1-y}Ba_yMnO_3$ (y<~0.2), *Phys. Rev. B* **64**, 134412 (2001).

[18] Radaelli, P.G., Iannone, G., Marezio, M., Hwang, H.Y., Cheong, S.-W., Jorgensen, J.D. & Argyriou, D.N., Structural effects on the magnetic and transport properties of perovskite $A_{1-x}A'_xMnO_3$ (x = 0.25, 0.30), *Phys. Rev. B* **56**, 8265 (1997).

[19] Alonso, J.A., Martínez-Lope, M.J., Casais, M.T., Aranda, M.A.G. & Fernández-Díaz, M.T., Metal-insulator transitions, structural and microstructural evolution of $RNiO_3$ (R = Sm, Eu, Gd, Dy, Ho, Y) perovskites: Evidence for room-temperature charge disproportionation in monoclinic $HoNiO_3$ and $YNiO_3$, *J. Am. Chem. Soc.* **121**, 4754 (1999).

[20] Garcia-Munoz, J.L., Fontcuberta, J., Suaaidi, M. & Obradors, X., Bandwidth narrowing in bulk $L_{2/3}A_{1/3}MnO_3$ magnetoresistive oxides, *J. Phys.: condens. Matter* **8**, L787 (1996).

[21] Ding, Y., Haskel, D., Tseng, Y.-C., Kaneshita E., van Veenendaal, M., Mitchell, J.F., Sinogeikin, S.V., Prakapenka, V. & Mao, H.-K., Pressure-induced magnetic transition in manganite ($La_{0.75}Ca_{0.25}MnO_3$), *Phys. Rev. Lett.* **102**, 237201 (2009).

[22] Zhai, X.F., Cheng, L., Liu, Y., Schlepütz, C.M., Dong, S., Li, H., Zhang, X.Q., Chu, S.Q., Zheng, L.R, Zhang, J., Zhao, A.D., Hong, H., Bhattacharya, A., Eckstein, J.N. & Zeng, C.G., Correlating interfacial octahedral rotations with magnetism in (LaMnO3+δ)N/(SrTiO3)N superlattices, Nature Commun. 5, 4283 (2014).

[23] Rondinelli, J.M. & Spaldin, N.A., Structure and properties of functional oxide thin films: Insights from electronic-structure calculations, *Adv. Mater.* **23**, 3363 (2011).

[24] Lee, J.H., Luo, G., Tung, I.C., Chang, S.H., Luo, Z., Malshe, M., Gadre, M., Bhattacharya, A., Nakhmanson, S.M., Eastman, J.A., Hong, H., Jellinek, J., Morgan, D., Fong, D. & Freeland, J.W., Dynamic layer rearrangement during growth of layered oxide films by molecular beam epitaxy, *Nature Mater.* **13**, 879 (2014).

[25] Rondinelli, J.M., May, S.J. & Freeland, J.W., Control of octahedral connectivity in perovskite oxide heterostructures: An emerging route to multifunctional materials discovery, *MRS Bull.* **37**, 261 (2012).

[26] Kinyanjui, M.K., Lu, Y., Gauquelin, N., Wu, M., Frano, A., Wochner, P., Reehuis, M., Christiani, G., Logvenov, G., Habermeier, H.-U., Botton, G.A., Kaiser, U., Keimer, B. & Benckiser, E., Lattice distortions and octahedral rotations in epitaxially strained $LaNiO_3/LaAlO_3$ superlattices, *Appl. Phys. Lett.* **104**, 221909 (2014).

[27] Borisevich, A.Y., Chang, H.J., Huijben, M., Oxley, M.P., Okamoto, S., Niranjan, M.K., Burton, J.D., Tsymbal, E.Y., Chu, Y.H., Yu, P., Ramesh, R., Kalinin, S.V. & Pennycook, S.J., Suppression of octahedral tilts and associated changes in electronic

properties at epitaxial oxide heterostructure interfaces, *Phys. Rev. Lett.* **105**, 087204 (2010).

[28] He, J., Borisevich, A.Y., Kalinin, S.V., Pennycook, S.J. & Pantelides, S.T., Control of octahedral tilts and magnetic properties of perovskite oxide heterostructures by substrate symmetry, *Phys. Rev. Lett.* **105**, 227203 (2010).

[29] Aso, R., Kan, D., Shimakawa, Y. & Kurata, H., Atomic level observation of octahedral distortions at the perovskite oxide heterointerface, *Sci. Rep.* **3**, 2214 (2013).

[30] Chen, Y.B, Sun H.P., Katz, M.B., Pan X.Q., Choi, K.J., Jang, H.W & Eom, C.B., Interface structure and strain relaxation in $BaTiO_3$ thin films grown on $GdScO_3$ and $DyScO_3$ substrates with buried coherent $SrRuO_3$ layer, *Appl. Phys. Lett.* **91**, 252906 (2007).

[31] Glazer, A.M., Classification of tilted octahedral in perovskites, *Acta Crystallogr., Sect. B: Struct. Sci.* **28**, 3384 (1972).

[32] Vasylechko, L., Akselrud, L., Morgenroth, W., Bismayer, U., Matkovskii, A. & Savytskii, D., The crystal structure of $NdGaO_3$ at 100 K and 293 K based on synchrotron data, *J. Alloys Compd.* **297**, 46 (2000).

[33] Liao, Z., Huijben, M., Koster, G. & Rijnders, G., Uniaxial magnetic anisotropy induced low field anomalous anisotropic magnetoresistance in manganite thin films, *Appl. Phys. Lett. Mater.* **2**, 096112 (2014).

[34] Ovsyannikov, S.V., Abakumov, A.M., Tsirlin, A.A, Schnelle, W., Egoavil, R., Verbeeck, J., Tendeloo, G.V., Glazyrin, K.V., Hanfland, M. & Dubrovinsk, L, Perovskite-like Mn_2O_3: a path to new manganites, *Angew. Chem. Int. Ed.* **52**, 1494 (2013).

[35] Boschker, H., Mathews, M., Houwman, E.P., Nishikawa, H., Vailionis, A., Koster, G., Rijnders, G. & Blank, D.H.A., Strong uniaxial in-plane magnetic anisotropy of (001)- and (011)-oriented $La_{0.67}Sr_{0.33}MnO_3$ thin films on $NdGaO_3$ substrates, *Phys. Rev. B* **79**, 214425 (2009).

[36] Macke, S., Radi, A., Hamann-Borrero, J.E, Verna, A., Bluschke, M., Brück, S., Goering E., Sutarto, R., He, F.Z., Cristiani, G., Wu, E., Benckiser, E., Habermeier, H.U., Logvenov, G., Gauquelin, N., Botton, G.A., Kajdos, A.P., Stemmer, S., Sawatzky, G.A., Haverkort, M.W., Keimer, B. & Hinkov, V., Element specific monolayer depth profiling, *Adv. Mater.* **26**, 6554 (2014).

[37] Park, J.H., Vescovo, E., Kim, H.J., Kwon, C., Ramesh, R. & Venkatesan, T., Magnetic properties at surface boundary of a half-metallic ferromagnet $La_{0.7}Sr_{0.3}MnO_3$, *Phys. Rev. Lett.* **81**, 1953 (1998).

[38] Huijben, M., Martin, L.W., Chu, Y.-H., Holcomb, M.B., Yu, P., Rijnders, G., Blank, D.H.A. & Ramesh, R., Critical thickness and orbital ordering in ultrathin $La_{0.7}Sr_{0.3}MnO_3$ films, Phys. Rev. B 78, 094413 (2008).

[39] Wang, B.M, You, L., Ren, P., Yin, X.M., Peng, Y., Xia, B., Wang, L., Yu, X.J., Poh, S.M., Yang, P., Yuan, G.L., Chen, L., Rusydi, A. & Wang, J.L., Oxygen-driven anisotropic transport in ultra-thin manganite films, *Nat. Commun.* **4**, 2778 (2013).

[40] Vailionis, A., Boschker, H., Siemons, W., Houwman, E.P., Blank, D.H.A., Rijnders, G. & Koster, G., Misfit strain accommodation in epitaxial ABO_3 perovskites: lattice rotations and lattice modulations, *Phys. Rev. B* **83** (6), 064101(2011).

[41] Medarde, M., Mesot, J., Lacorre, P., Rosenkranz, S., Fischer, P. & Gobrecht, K., High-pressure neutron-diffraction study of the metallization process in $PrNiO_3$, *Phys. Rev. B* **52**, 9248 (1995).

[42] Dong, S., Yunoki, S., Zhang, X., Şen, C., Liu, J.-M. & Dagotto, E., Highly anisotropic resistivities in the double-exchange model for strained manganites, *Phys. Rev. B* **82**, 159902 (2010).

[43] Macke, S. & Goering, E., Magnetic reflectometry of heterostructures, *J. Phys.: Condens. Matter* **26**, 363201, (2014).

[44] Hawthorn, D.G., He, F., Venema, L., Davis, H., Achka, A.J., Zhang, J., Sutarto, R., Wadati, H., Radi, A., Wilson, T., Wright, G., Shen, K.M., Geck, J., Zhang, H., Novák, V. & Sawatzky, G.A., An in-vacuum diffractometer for resonant elastic soft x-ray scattering, *Rev. of Sci. Instrum.* **82**, 073104 (2011).

[45] Zhong, Z., Toth, A. & Held, K., Theory of spin-orbit coupling at $LaAlO_3/SrTiO_3$ interfaces and $SrTiO_3$ surfaces, *Phys. Rev. B* **87**, 161102 (2013).

[46] Yamasaki, A., Feldbacher, M., Yang, Y.-F., Andersen, O.K. & Held, K., Pressure-induced metal-insulator transition in $LaMnO_3$ is not of Mott-Hubbard type, *Phys. Rev. Lett.* **96**, 166401 (2006).

[47] Daisuke Kan et al. Tuning magnetic anisotropy by interfacially engineering the oxygen coordination environment in a transition-metal oxide. Nature Mater. (accepted)

Acknowledgements

We would like to acknowledge Dr. Evert Houwman for stimulated discussion. M.H., G.K. and G.R. acknowledge funding from DESCO program of the Dutch Foundation for Fundamental Research on Matter (FOM) with financial support from the Netherlands Organization for Scientific Research (NWO). This work was funded by the European Union Council under the 7th Framework Program (FP7) grant nr NMP3-LA-2010-246102 IFOX. J.V. and S.V.A. acknowledges funding from FWO project G.0044.13N and G. 0368.15N. The Qu-Ant-EM microscope was partly funded by the Hercules fund from the Flemish Government. N.G. acknowledges funding from the European Research Council under the 7th Framework Program (FP7), ERC Starting Grant 278510 VORTEX. N.G., S.V.A., J.V. and G.V.T. acknowledge financial support from the European Union under the Seventh Framework Program under a contract for an Integrated Infrastructure Initiative (Reference No. 312483-ESTEEM2). The Canadian work was supported by NSERC and the Max Planck-UBC Centre for Quantum Materials. Some experiments for this work were performed at the Canadian Light Source, which is funded by the Canada Foundation for Innovation, NSERC, the National Research Council of Canada, the Canadian Institutes of Health Research, the Government of Saskatchewan, Western Economic Diversification Canada, and the University of Saskatchewan. Z.Z. acknowledges funding from the SFB ViCoM (Austrian Science Fund project ID F4103-N13), and Calculations have been done on the Vienna Scientific Cluster (VSC).

Author Contributions

Z.L. concept design, film growth and magnetic/transport measurements. Data analysis and interpretation: Z.L., M.H., G.K., G.R., Z.Z; STEM and EDX measurements and analysis: N.G., S.V.A., J.V., G.V.T; RXR measurements and analysis: S. M., G. K., R.J.G., G.A.S.; DFT calculations: Z.Z., K.H; All authors extensively discussed the results and were involved in writing of the manuscript.

Additional information

Supplementary information is available in the online version of the paper. Reprints and permissions information is available online at www.nature.com/reprints. Correspondence and requests for materials should be addressed to M.H.

Competing financial interest

The authors declare no competing financial interests.

Figures and Figure captions:

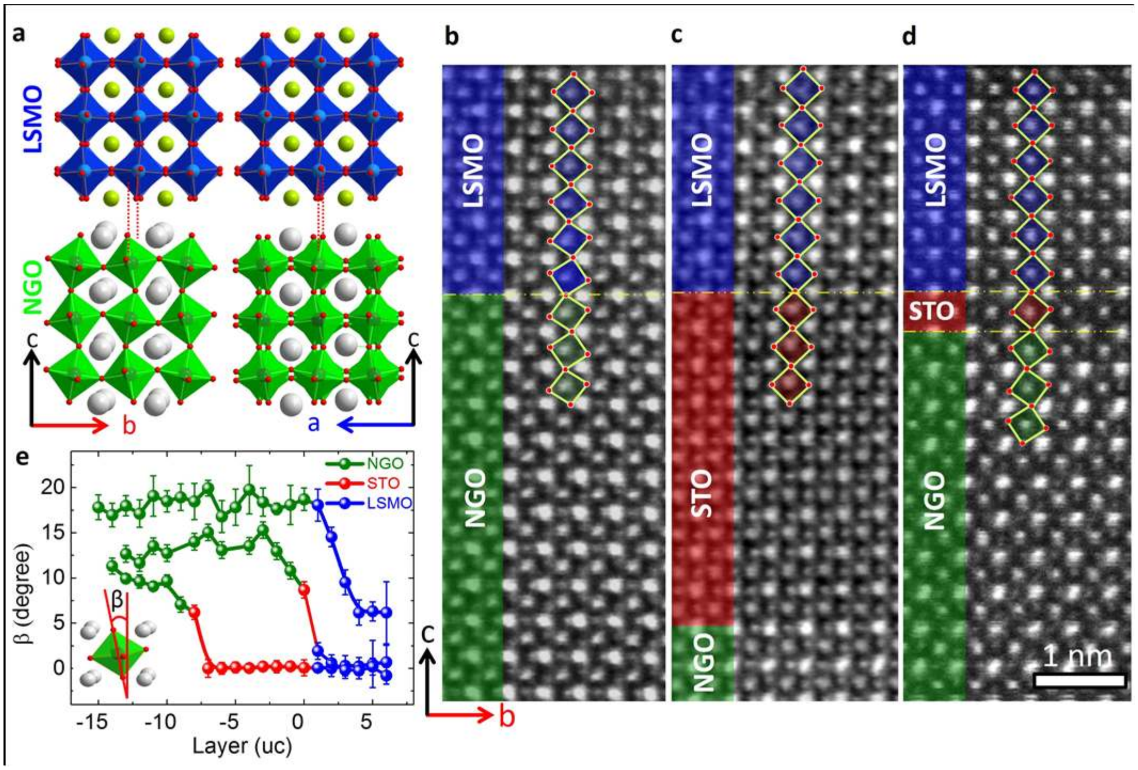

Figure 1 | Oxygen octahedral coupling at interfaces in manganite heterostructures. a, Schematic models of atomic ordering in LSMO and NGO crystal structures. Inversed annular bright-field STEM images of (**b**) LSMO/NGO, (**c**) LSMO/STO (9 uc)/NGO and (**d**) LSMO/STO (1 uc)/NGO heterostructures. The oxygen atoms are clearly visible, and the connectivity of oxygen octahedra across the interfaces is indicated. All the LSMO films are 6 uc thick. **e**, Layer-position dependent mean octahedral tilt angle (β) together with their standard deviation in LSMO/NGO heterostructures with and without a STO buffer layer. The data for non-buffered sample is shifted upward by 6^o for clarity.

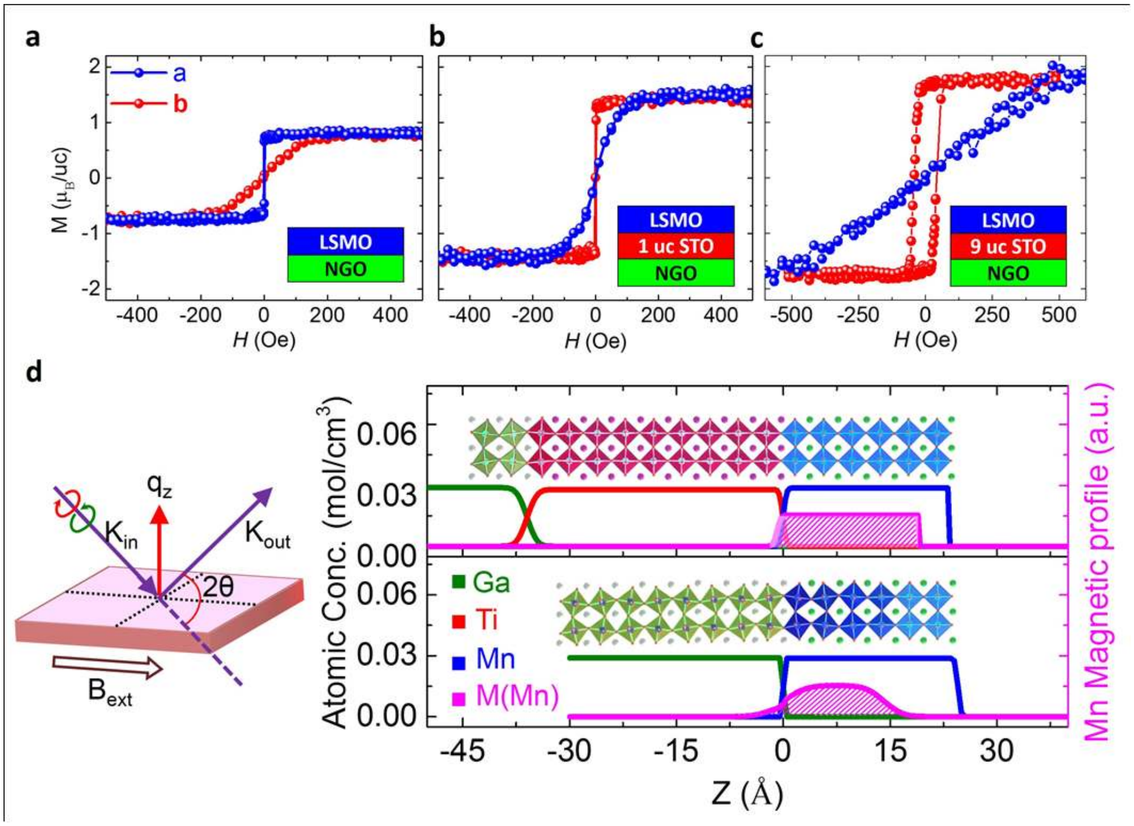

Figure 2 | Magnetic anisotropy in manganite heterostructures. The M-H curves at 100 K along *a* and *b*-axis of the 6 uc LSMO films on NGO substrates without (**a**) and with a 1 uc (**b**) and 9 uc (**c**) STO buffer layer. (**d**) RXR measurements of 6 uc LSMO films with (top panel) and without (bottom panel) a 9 uc STO buffer layer showing depth profiles of the Ga, Ti, Mn atomic concentration (resp. green, red and blue lines) and Mn magnetization (M, purple line with shaded area) at 20 K. Schematic shows experimental setup to perform RXR measurement where a 0.6 T magnetic field was applied in-plane along magnetic easy axis during the measurement. Atomic structure profiles along out of plane direction (Z), according to Fig. 1b-c, are also shown for comparison.

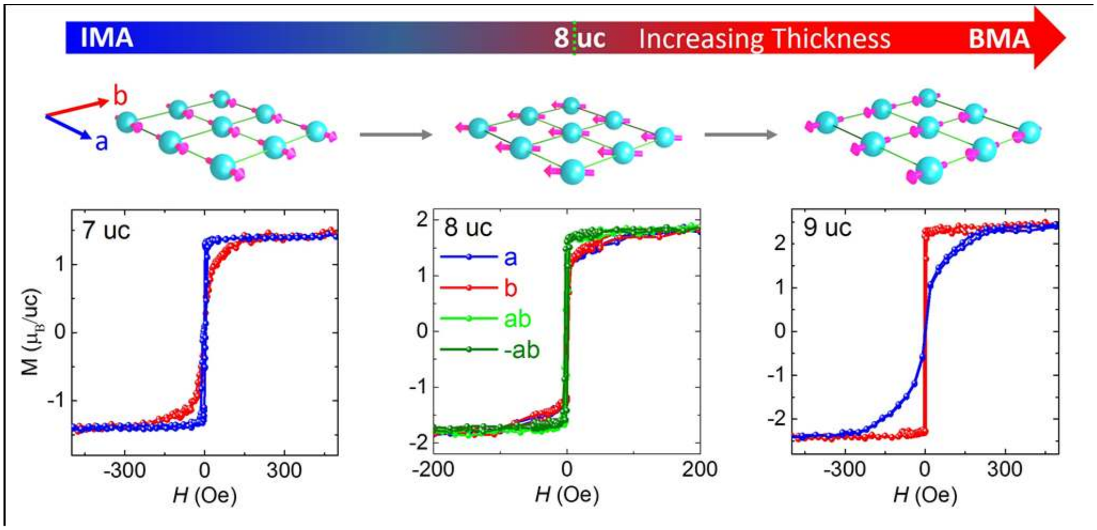

Figure 3 | Thickness dependence of the magnetic anisotropy in manganite heterostructures. The M-H curves at 100 K along *a*- and *b*-axis of the LSMO films with thicknesses of 7, 8 and 9 uc on NGO substrates. The schematics at the top show the corresponding ground state of the Mn spin orientation.

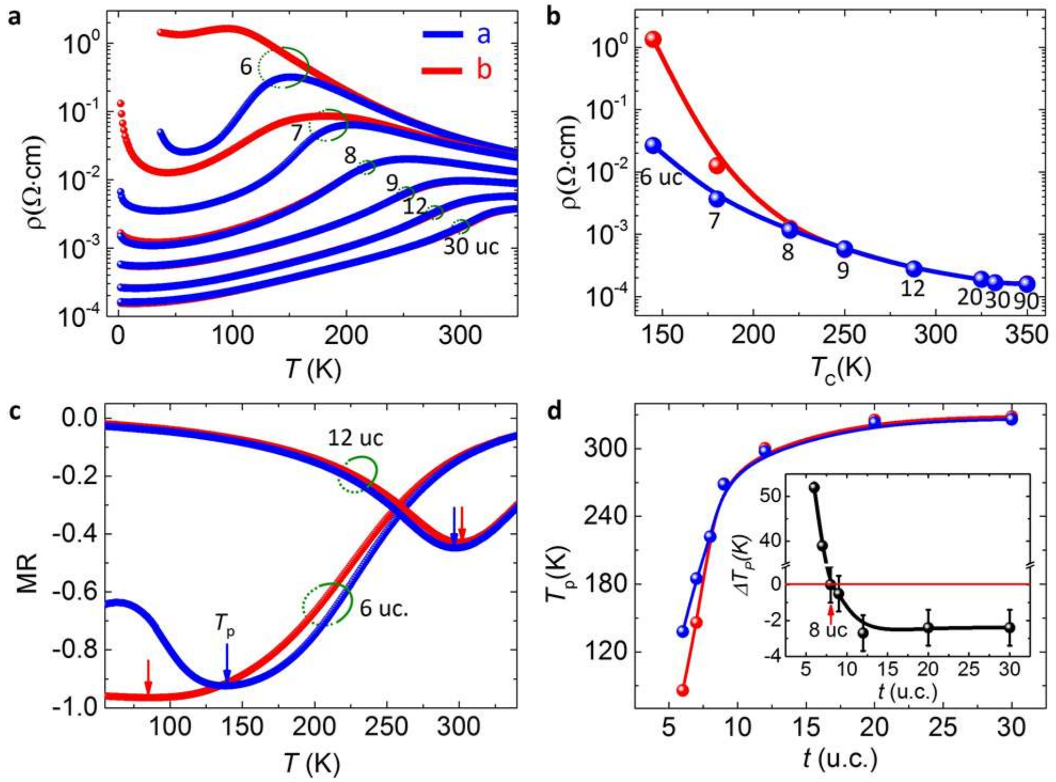

Figure 4 | Thickness dependence of the transport anisotropy in manganite heterostructures. **a**, Temperature dependent resistivity along *a* and *b*-axis for different LSMO thickness from 6 to 30 uc. Resistivity curves for the same thickness are grouped by the green circles. **b**, Curie temperature dependent resistivity at 50 K along the *a* and *b*-axis. The corresponding thickness is marked at each data point. **c**, Temperature dependent magnetoresistance MR=(R(B)-R(0))/R(0) along *a* and *b*-axis under out of plane 9 T magnetic field for 6 and 12 uc LSMO films. Resistivity curves for the same thickness are grouped by the green circles. The arrows indicate the position of T_p. **d**, T_p versus LSMO film thickness along *a* and *b*-axis. Inset, $\Delta T_p = T_p(a) - T_p(b)$ versus LSMO film thickness. The error bars are temperature uncertainty due to temperature ramping step length. Data measured along the *a*-axis is indicated in blue in all 4 figures, while data along *b*-axis is indicated in red.

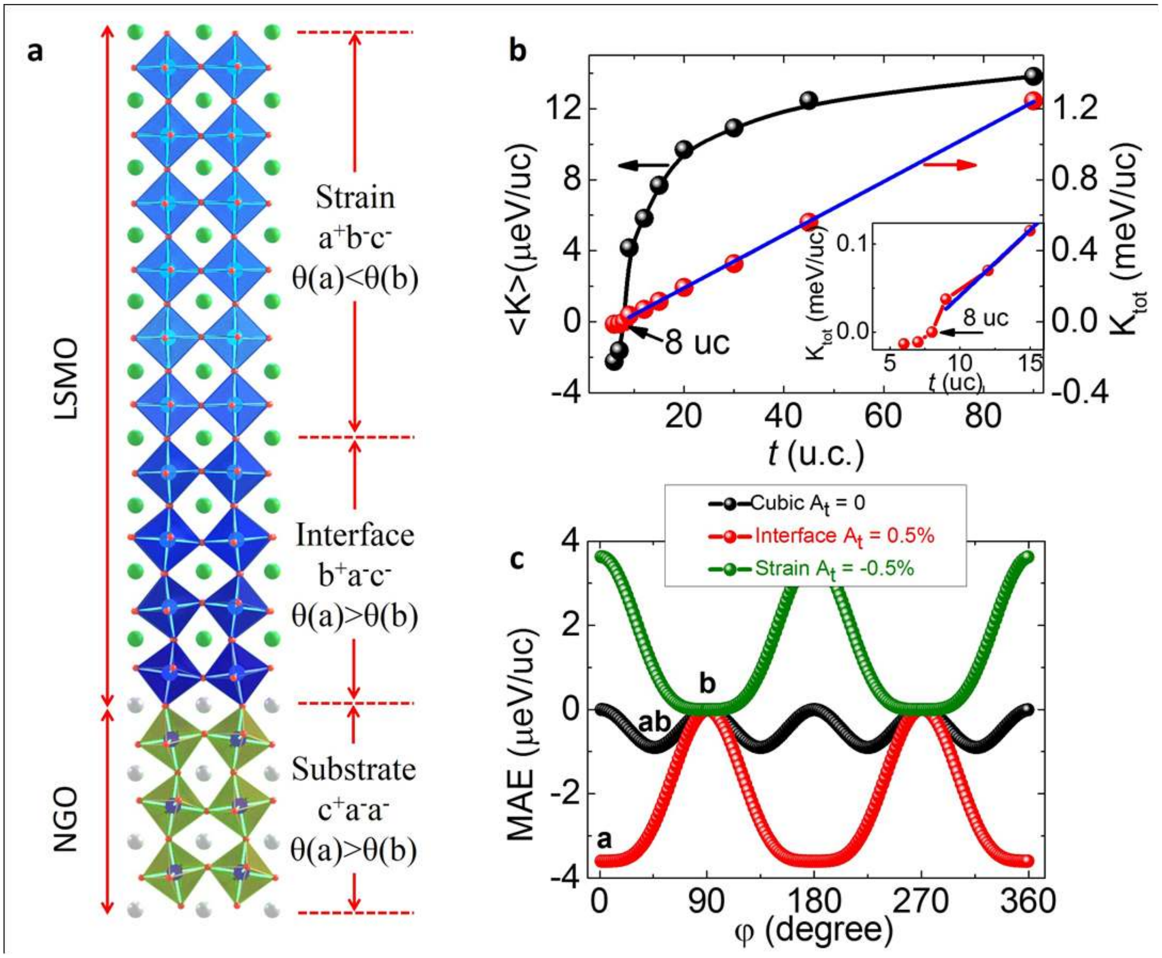

Figure 5 | Structural mechanism of directional switching of magnetic anisotropy. a, Structural evolution along the out-of-plane direction of the LSMO thin film on a NGO substrate. **b**, Film thickness dependence of the anisotropic energy constant <*K*> and total anisotropic energy constant K_{tot} at 50 K. The blue line is resultant linear fitting of the K_{tot} vs. t in t > 8 uc region. Inset: Zoom in of K_{tot} vs t curve including the linear fitting result around t = 8 uc. **c**, Tight binding simulations of the anisotropy energy of a LSMO monolayer with different asymmetric hopping factor A_t ($= 1 - t_0(\vec{b})/t_0(\vec{a})$): 0% (cubic LSMO, black), 0.5% (interfacial LSMO on NGO, red), -0.5% (strained bulk LSMO on NGO, green).

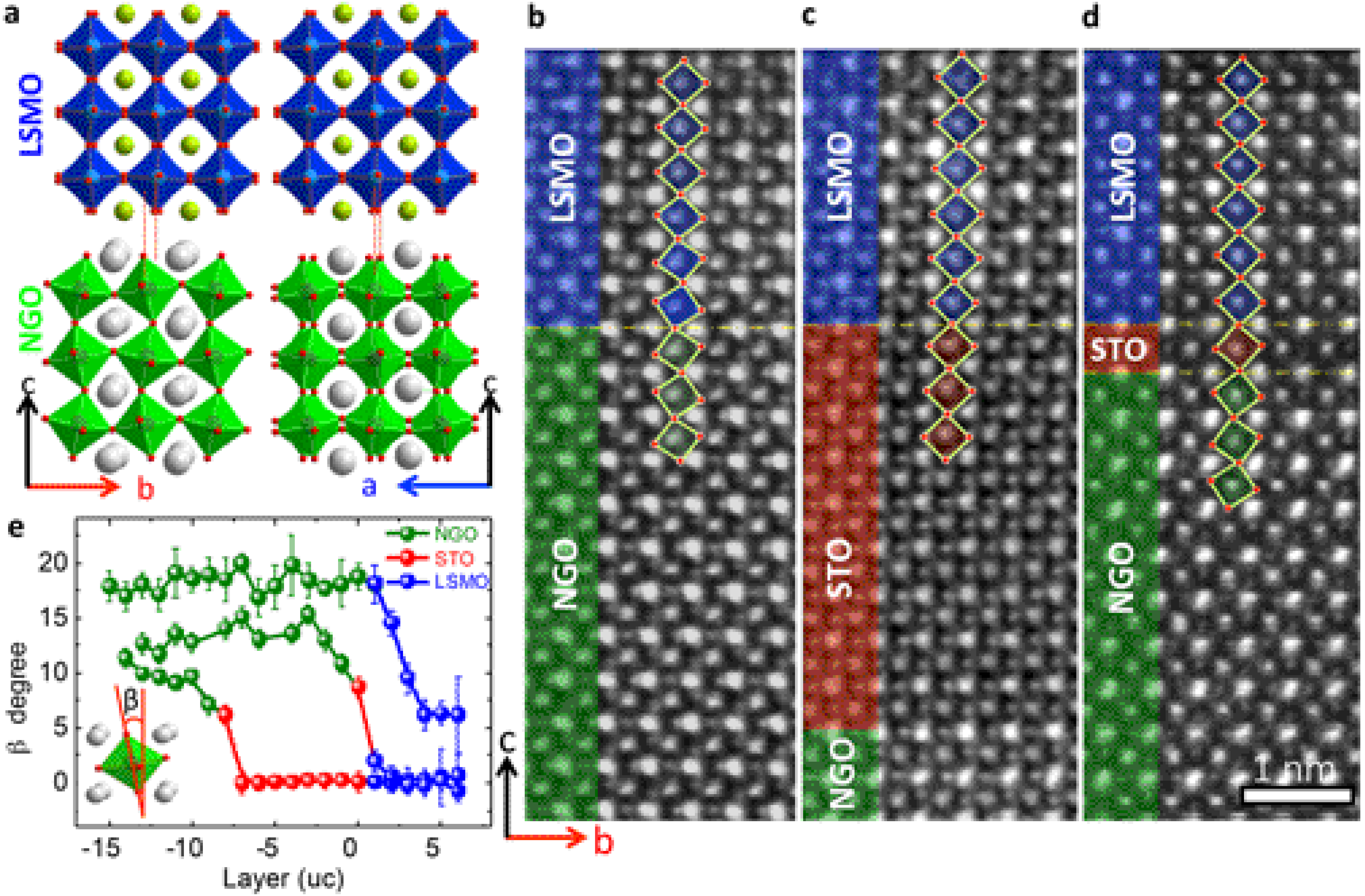
a
LSMO
NGO
c
b
c
a
b
c
d
LSMO
NGO
LSMO
STO
NGO
LSMO
STO
NGO
1 nm
c
b
e
NGO
STO
LSMO
β degree
β
20
15
10
5
0
-15
-10
-5
0
5
Layer (uc)

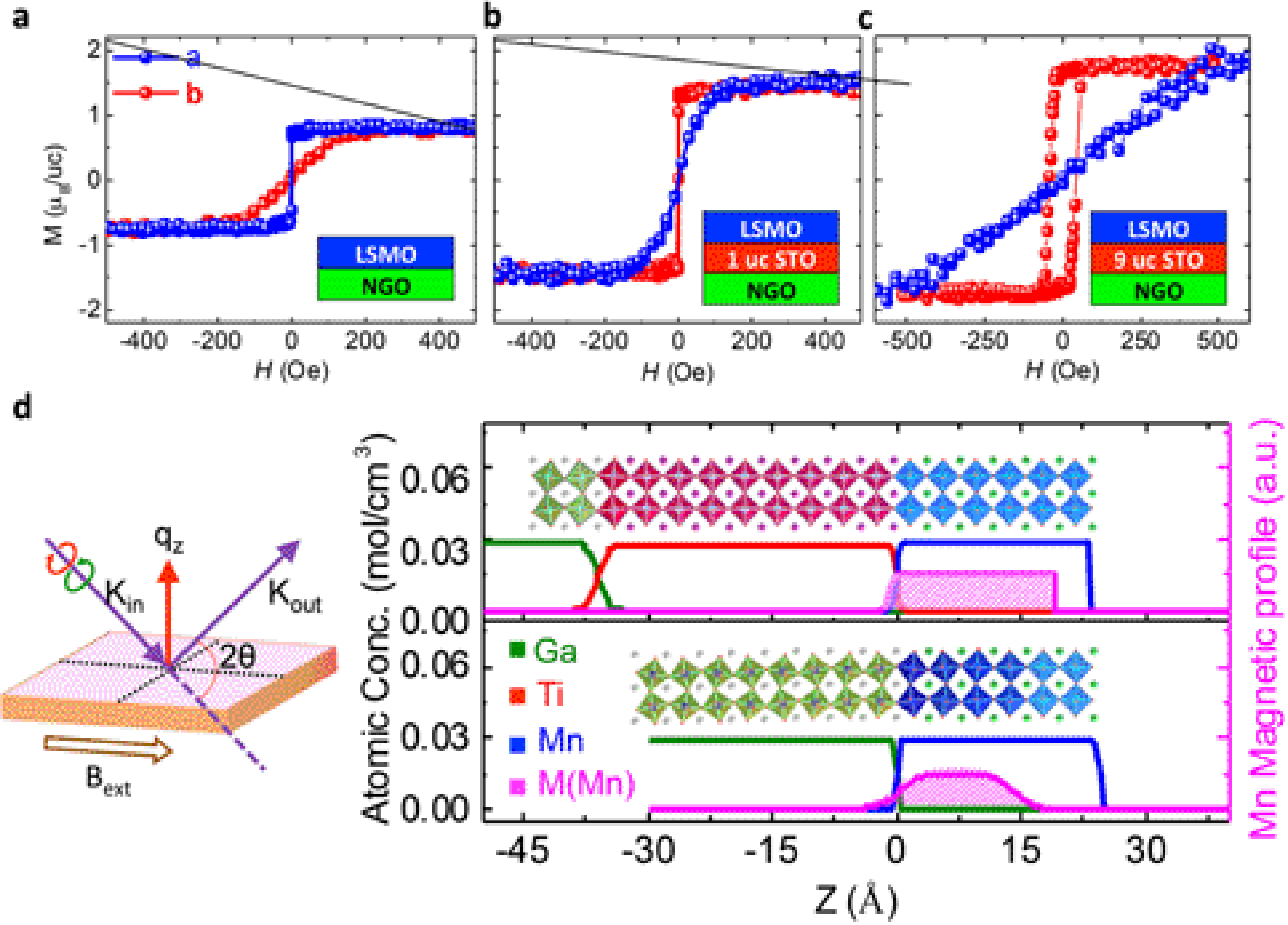
a
b
c
d
M (μ_B/uc)
H (Oe)
-400
-200
0
200
400
-500
-250
250
500
2
1
0
-1
-2
a
b
LSMO
NGO
1 uc STO
9 uc STO
q_z
K_{in}
K_{out}
2θ
B_{ext}
Atomic Conc. (mol/cm^3)
Mn Magnetic profile (a.u.)
0.06
0.03
0.00
Ga
Ti
Mn
M(Mn)
-45
-30
-15
0
15
30
Z (Å)

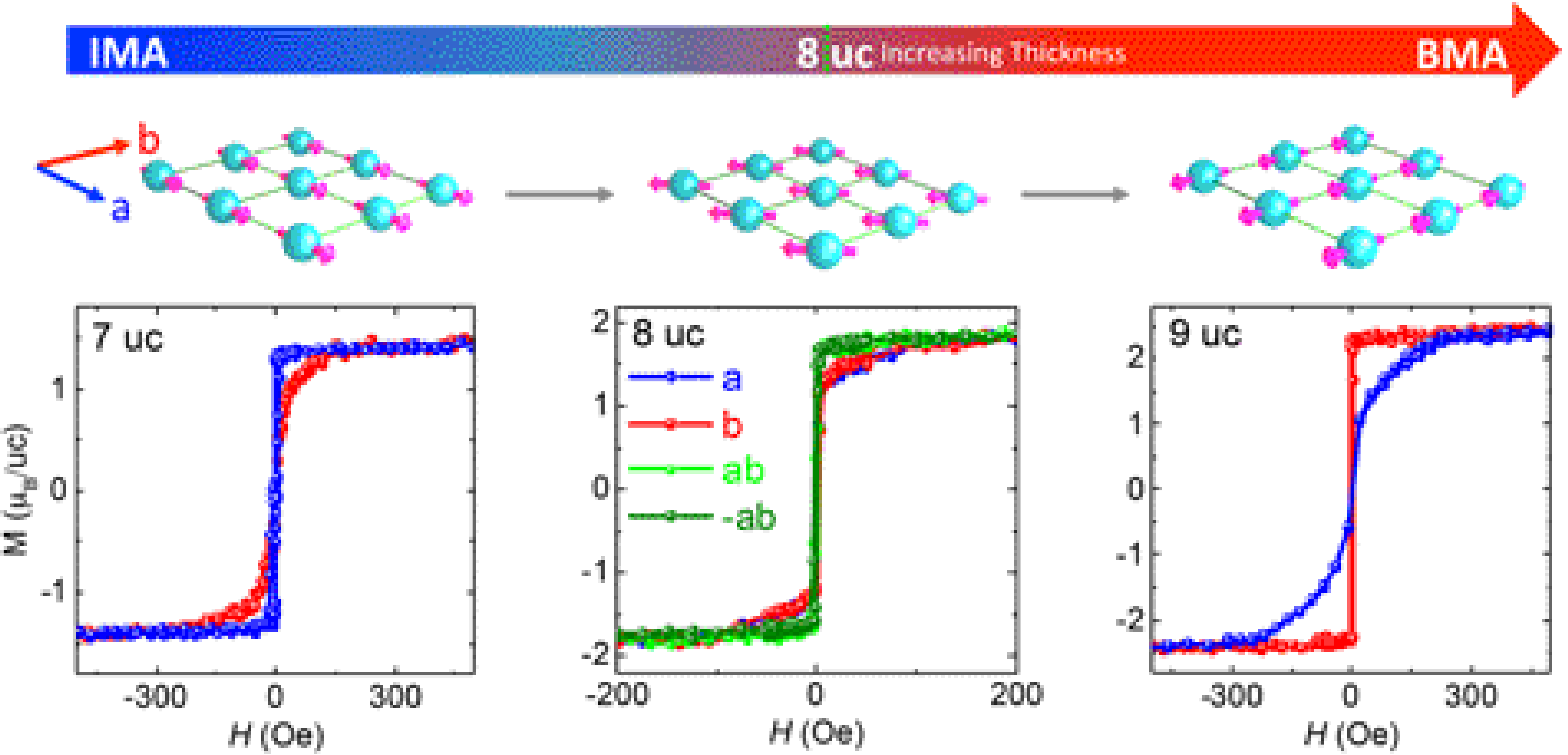
IMA
8 uc
Increasing Thickness
BMA
b
a
7 uc
M (μ_B/uc)
1
0
-1
-300
0
300
H (Oe)
8 uc
a
b
ab
-ab
2
1
0
-1
-2
-200
0
200
H (Oe)
9 uc
2
1
0
-1
-2
-300
0
300
H (Oe)

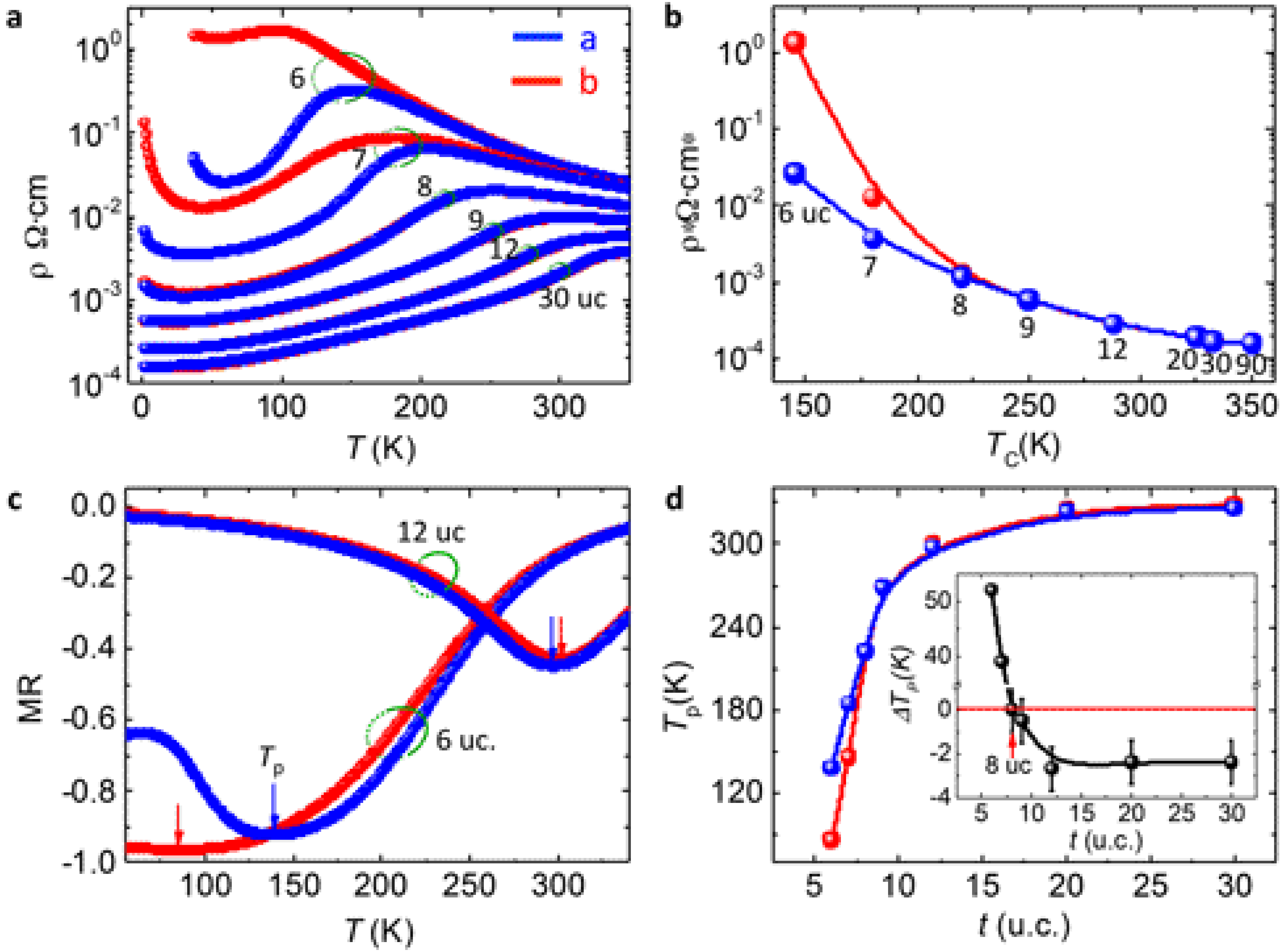
a
b
c
d
a
b
ρ Ω·cm
10^0
10^{-1}
10^{-2}
10^{-3}
10^{-4}
6
7
8
9
12
30 uc
0
100
200
300
T (K)
ρ Ω·cm
6 uc
7
8
9
12
20
30
90
150
200
250
300
350
T_C(K)
MR
0.0
-0.2
-0.4
-0.6
-0.8
-1.0
12 uc
6 uc.
T_p
100
150
200
250
300
T (K)
T_p(K)
300
240
180
120
5
10
15
20
25
30
t (u.c.)
ΔT_p(K)
50
40
0
-2
-4
8 uc
5
10
15
20
25
30
t (u.c.)

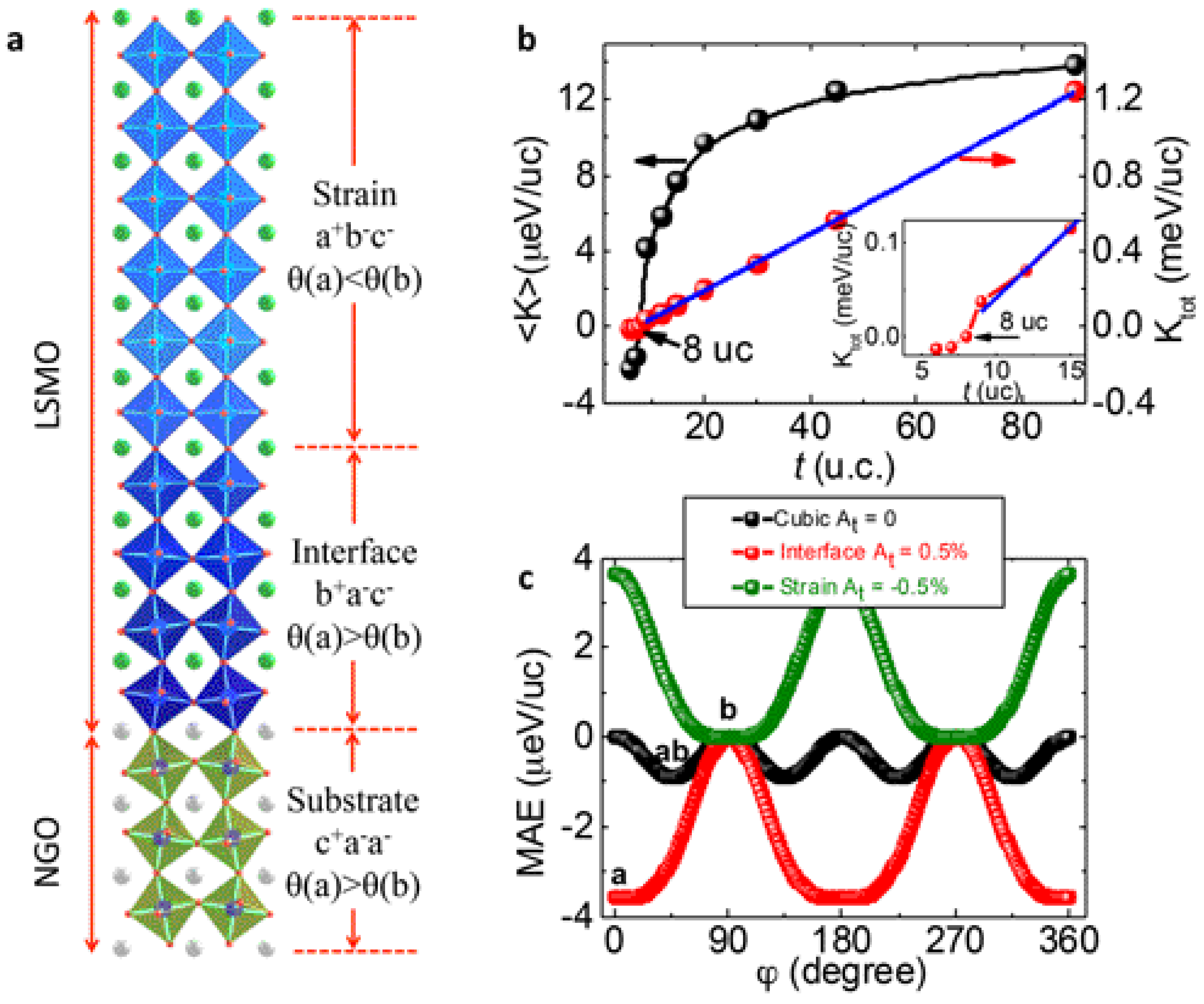
a
LSMO
NGO
Strain
a⁺b⁻c⁻
θ(a)<θ(b)
Interface
b⁺a⁻c⁻
θ(a)>θ(b)
Substrate
c⁺a⁻a⁻
θ(a)>θ(b)
b
<K> (μeV/uc)
K_tot (meV/uc)
t (u.c.)
8 uc
-4
0
4
8
12
20
40
60
80
-0.4
0.0
0.4
0.8
1.2
K_tot (meV/uc)
0.0
0.1
5
10
15
t (uc)
8 uc
c
Cubic A_t = 0
Interface A_t = 0.5%
Strain A_t = -0.5%
MAE (μeV/uc)
φ (degree)
-4
-2
0
2
4
0
90
180
270
360
a
b
ab

Supplementary information:

Controlled lateral anisotropy in correlated manganite heterostructures by interface-engineered oxygen octahedral coupling

Z. Liao[1], M. Huijben[1*], Z. Zhong[2], N. Gauquelin[3], S. Macke[4,5], R. J. Green[4,6], S. van Aert[3], J. Verbeeck[3], G. Van Tendeloo[3], K. Held[2], G. A. Sawatzky[4], G. Koster[1] & G. Rijnders[1]

[1]*MESA+ Institute for Nanotechnology, University of Twente, P.O.BOX 217, 7500 AE, Enschede, The Netherlands*

[2]*Institute of Solid State Physics, Vienna University of Technology, A-1040 Vienna, Austria*

[3]*Electron Microscopy for Materials Science (EMAT), University of Antwerp, 2020 Antwerp, Belgium*

[4]*Quantum Matter Institute and Department of Physics and Astronomy, University of British Columbia, 2355 East Mall, Vancouver, V6T 1Z4, Canada*

[5]*Max Planck Institute for Solid State Research, Heisenbergstraße 1, 70569 Stuttgart, Germany*

[6]*Max Planck Institute for Chemical Physics of Solids, Nöthnitzerstraße 40, 01187 Dresden, Germany*

1. Growth of $La_{2/3}Sr_{1/3}MnO_3$ and $SrTiO_3$ films

The $La_{2/3}Sr_{1/3}MnO_3$ (LSMO) and $SrTiO_3$ (STO) films were grown by pulsed laser deposition (PLD) in a layer by layer fashion as shown in Figure S1a. The thickness of the LSMO and STO was controlled by counting the RHEED oscillations, enabling a precise unit cell (uc) control of the growth. The surface morphology was characterized by atomic force microscopy (AFM), which showed atomic flat surface of the LSMO films with clear one unit cell height terrace steps (see Figure S1b-c). RHEED pattern of a 30 uc LSMO film, as shown in the inset of Figure S1c, also indicates a 2D smooth surface.

---

[*] email: m.huijben@utwente.nl

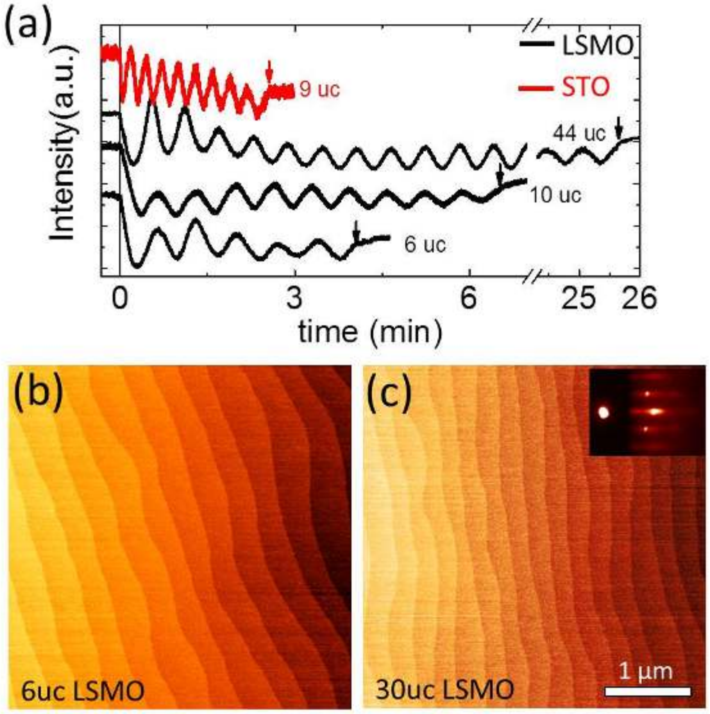

Figure S1 | Growth and characterization of LSMO and STO films. **a,** RHEED intensity oscillations during the growth of LSMO (6, 10, 44 uc) and STO (9 uc). The growth started at t = 0 and stopped at the time indicated by arrows. AFM images of 6 uc **(b)** and 30 uc **(c)** LSMO layers.

2. X-ray reciprocal space mapping of $La_{2/3}Sr_{1/3}MnO_3$ and $SrTiO_3$ films

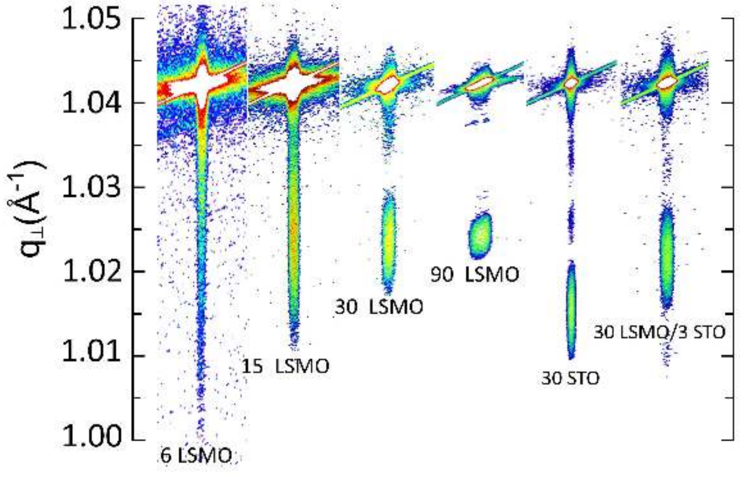

Figure S2 | X-ray reciprocal space mapping of (620) peaks for different thicknesses (6, 15, 30, 90 uc) of LSMO films, 30 uc STO and 30 uc LSMO with 3 uc STO buffer layer on $NdGaO_3$ (110) substrates. The thickness in unit of unit cell is indicated near the peak.

Due to a very small lattice mismatch (0.4%) between the LSMO and NGO crystal structures, the LSMO layer is easily strained to the NGO substrate as confirmed by X-ray diffraction (XRD) measurements, which were performed using a PANalytical X'Pert Materials Research Diffractometer (MRD) in high resolution mode. Reciprocal space mapping (RSM) of (260), (444), (620) and (44-4) diffraction peaks has been performed at room temperature. Figure S2 only shows (620) peaks as examples. According to RSM, the LSMO films ranging from 4 unit cell (uc) to 90 uc have same in-plane lattice constants with $NdGaO_3$ (NGO) substrates, indicating that all films are fully strained to the substrates regardless of film thickness. The STO buffer layer is fully strained to the NGO substrate as indicated by the RSM of a 30 uc STO film on a NGO substrate. For STO-buffered LSMO, it is found that the LSMO layers are still fully strained to the NGO substrates. Therefore, with or without STO buffer layer, the in-plane lattice constants (*a* and *b*) of LSMO maintain constant.

3. Electron Energy Loss Spectroscopy maps and estimation of oxygen octahedral tilt angle

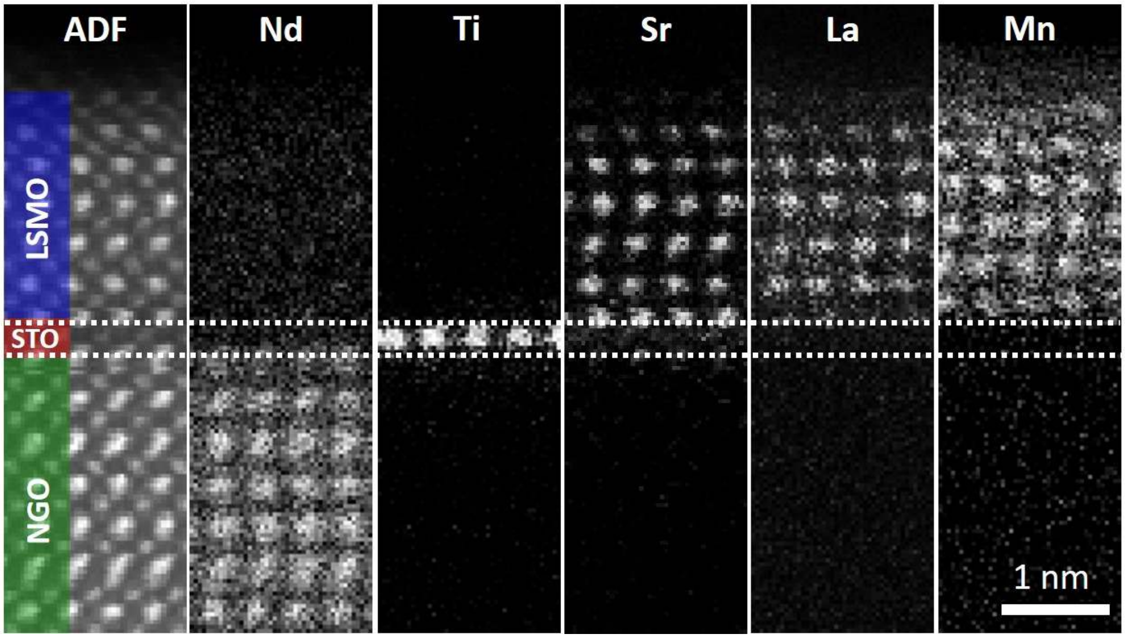

Figure S3 | Atomically resolved EELS mapping of Nd $M_{4,5}$, Ti $L_{2,3}$, Sr $L_{2,3}$, La $M_{4,5}$, and Mn $L_{2,3}$ at the 1 uc STO buffered 6 uc LSMO on NGO (110) heterostructure. The first panel is the simultaneously acquired annular dark field (ADF) image.

The interfacial atomic ordering in LSMO/NGO and LSMO/STO/NGO heterostructures is determined by performing both electron energy loss spectroscopy (EELS) and energy-dispersive X-ray spectroscopy (EDX) mapping across the interfaces. An example of atomically resolved EELS mapping of different elements in 1 uc STO buffered 6 uc LSMO film on NGO (110) is shown in Figure S3 and enables the characterization of the atomic ordering in the interface region. The mapping of Ga is not possible by EELS due to the fact that Ga is a very broad-edge in the region from 1100 to 1500eV, where the Nd $M_{1,2,3}$ has an important spectral weight and is therefore not displayed. Chemically sharp interfaces are indicated by the EELS mapping. A Ti monolayer without local intermixing is observed between LSMO film and NGO substrate confirming the abruptness of the interfaces.

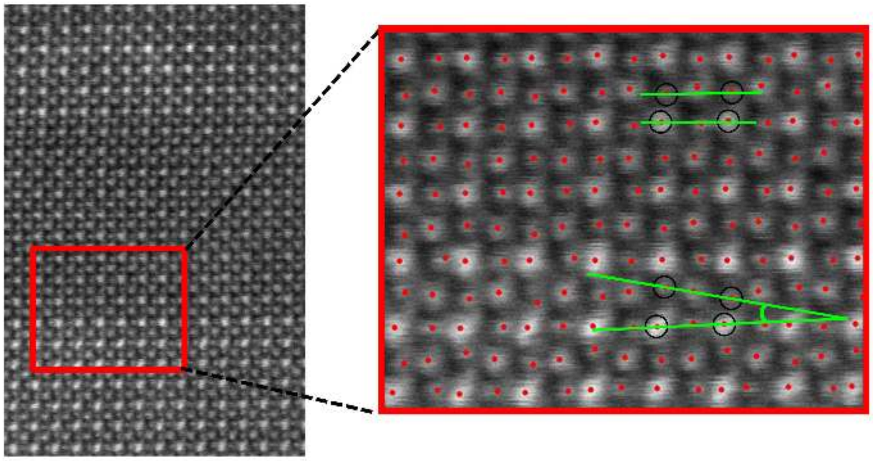

Figure S4 | Estimation of the oxygen octahedral tilt angle. Inversed ABF-STEM image of a LSMO/STO/NGO samples (left) and its enlarged view of the boxed region (right). The STO and LSMO are 9 uc and 6 uc thick, respectively. Small red dots are estimated atomic columns positions.

To study the layer-position dependent octahedral tilt angle, inversed Annular Bright-Field scanning transmission electron microscopy (ABF-STEM) images as indicated in Figure S4 as an example have been quantified by statistical parameter estimation theory. Using this method, the experimental image intensities are modelled by a superposition of Gaussians functions peaked at the atomic column positions. The parameters of this model, including the atomic column positions, the height and width of the Gaussian peaks, have been determined using the least squares estimator [1-3]. From the estimated atomic column positions, the BO_6 octahedral tilt angles (β) (B being either Ga, Ti or Mn depending on the layer) have been determined as illustrated in the inversed ABF image of the LSMO/STO/NGO cross-section in Figure S4. From the estimated atomic column positions, shown in red dots in the right panel of Figure S4, the tilt of each octahedron has been determined by measuring the angle between two straight lines crossing pairs of heavy columns and pairs of light O columns. With this method, the layer position dependent mean values of these tilt angles together with their standard deviation on the mean have been determined and are shown Figure 1e in main text.

4. Magnetization architecture by engineering interfacial oxygen octahedral coupling

The capability to rotate the easy axis in-plane by controlled interface octahedral coupling allows us to realize non-collinear magnetization in a LSMO/STO/LSMO/NGO magnetic tunneling junction (MTJ). Figure S5a shows an example of a MTJ with orthogonal magnetic easy axes between top LSMO and bottom LSMO layers. As shown in Figure S5a, the M-H curve along [001]-axis of the LSMO/STO/LSMO/NGO MTJ is a combination of hard axis M-H curve from top LSMO layer and easy axis M-H curve from bottom LSMO layer. This scenario is confirmed when we fully removed the top LSMO layer by wet-etching with 20wt% HCl acid and measured the M-H again. The contribution to the total M-H curve from the bottom LSMO layer doesn't change after fully etching away the top LSMO layer. The M-H curve of the bottom LSMO layer also proves that it has an easy axis along [001] direction. By subtracting the magnetization of the bottom LSMO layer, we can extract the magnetization of the top LSMO layer (blue curve in Figure S5a), which shows a typical hard axis M-H characteristic. Therefore the easy axis for the top LSMO layer is along [1-10] direction.

By patterning the STO buffer layer, we are able to locally vary the magnetic properties. As shown in Figure S5b, we fabricated a patterned STO layer by using a shadow mask during growth. After in-situ removing the shadow mask, a 6 uc LSMO film was subsequently grown on the patterned STO layer. The M-H curve of such sample as shown in Figure S5b shows a typical combination of hard axis M-H curve from the LSMO/STO/NGO region and easy axis M-H curve from the LSMO/NGO region.

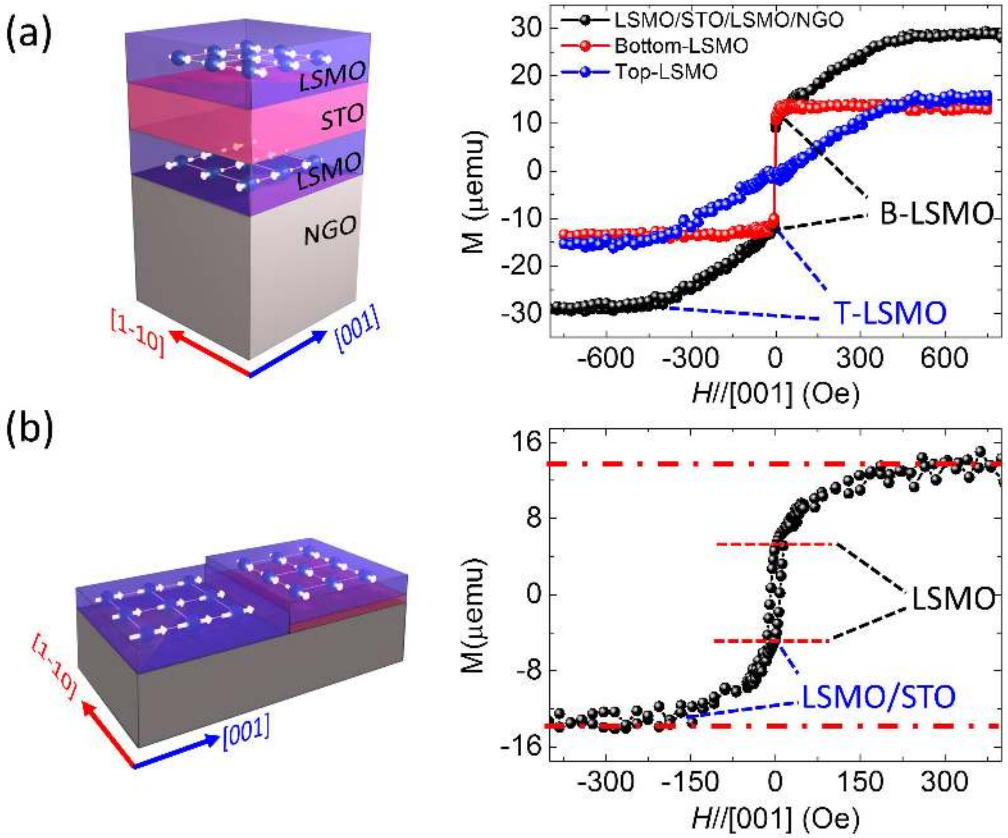

Figure S5 | Magnetization architecture in out of plane and in-plane directions. a, Orthogonal magnetization in LSMO(6uc)/STO(8uc)/LSMO(6uc)/NGO magnetic tunneling junction**.** Left, the schematic spin configuration of bottom LSMO (B-LSMO) and top LSMO (T-LSMO) layers. Right, M-H curves along [001] axis for as-grown (AG) sample (black curve), and top LSMO fully etched (TLE) sample (red curve) and extracted magnetization of top LSMO layer (green curve) by subtracting TLE from AG (AS-TLE). The M-H curves were measured at 150 K. **b,** In-plane magnetization patterning. Left panel shows the LSMO film on patterned STO buffer layer. The STO buffer layer (red) in left panel is 1 uc thick and the LSMO film (blue) is 6 uc thick everywhere. Right panel shows the M-H curve along [001] direction at 75 K.

5. Determination of the magneto-optical profile of Mn

The magneto-optical profile was determined by x-ray resonant magnetic reflectivity (XRMR) [4]. An element-specific continuum model was used to construct an energy and depth dependence refractive index [5]. The optical constants of Mn, La and Nd were taken from XAS signals and fitted to off-resonant tables, and for all other elements the tabulated values were used [6].

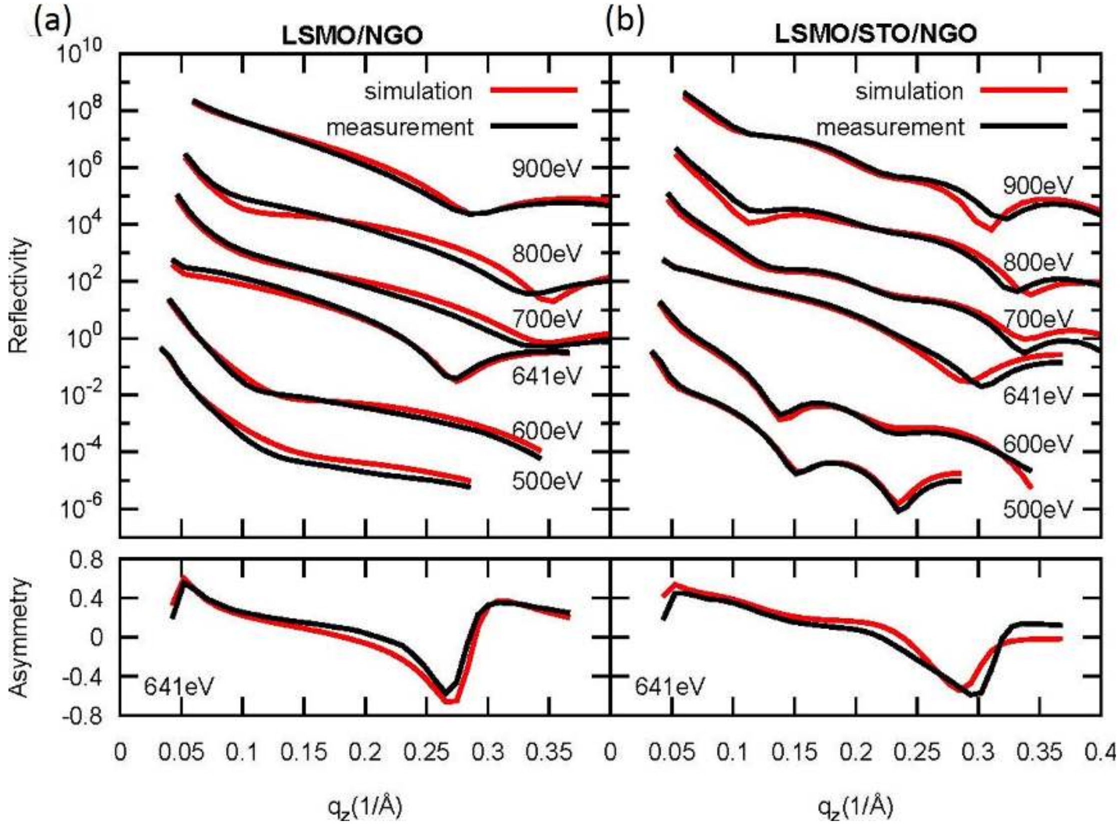

Figure S6 | Measured and simulated reflectivity curves for (a) LSMO/NGO and (b) LSMO/STO/NGO (b) at 20 K. The structural fit was performed using the off-resonant energies. For clarity the reflectivity curves are scaled. The magnetic profile (bottom) was determined on the L_3 edge of Mn at 641 eV by the asymmetry signal between left and right circular polarized light with an applied magnetic field along the scattering plane.

The chemical depth profile is determined using reflectivity curves measured at off-resonant energies, utilizing the optical contrast before and after each resonance. The film thickness, roughness, and a small contamination of light elements were taken as fit parameters, while the concentrations of the NGO, STO, and LSMO elements were fixed at stoichiometric values. Figure S6 shows the corresponding measurements and fits, which were performed using the software ReMagX [6,7]. Soft X-Ray Reflectivity of a 6 uc LSMO film with and without a STO buffer layer shows similar behavior to hard X-Ray Reflectivity, strongly indicating the high quality of our LSMO and STO films.

After determining the chemical profile, further measurements and modeling were used to determine the magneto-optical depth profile. For these measurements, a permanent magnet array producing a homogenous 0.6 Tesla field was inserted in the sample environment, aligning the magnetization in the film xy plane along the measurement scattering plane. Two different reflectivity curves at the Mn L_3 resonance were measured by using left R_l and right circular R_r polarized light. Figure S6 (bottom) shows the asymmetry defined as $A = (R_l-R_r)/(R_l+R_r)$ and the corresponding fit. During fitting, the magnetic depth profile was assumed to be one homogeneous magnetic layer with in-plane magnetization and free thickness, position and magnetic roughness. As model inputs, the magneto optical constants were determined by the XMCD spectra taken from [8].

The magnetic profile obtained from XRMR is consistent with magnetization measured by Quantum Design Vibrating Sample Magnetometer (QD-VSM). At 50 K, the saturated magnetic moment from VSM for a 6 uc LSMO film with a 9 uc STO buffer layer is 2.29 μ_B/Mn while for a non-buffered 6 uc LSMO film it is 1.57 μ_B/Mn, so their ratio is 1.46. Comparing with the estimated ratio of ~1.43 from the magnetic profile, as shown in Figure 2d in main text, they are self-consistent.

6. Characterization of transport properties

A van-der-Pauw geometry, as shown in Figure S7a, is utilized to measure the anisotropic transport properties [9]. The $R_{[001]} = V_{24}/I_{13}$ and $R_{[1-10]} = V_{12}/I_{34}$ are simultaneously measured during the temperature variations. As shown in Figure S7b**,** the T_P in temperature dependent the MR curve increases with increasing thickness. The LSMO film with higher T_P exhibits a lower MR effect. The maximum |MR|, which occurs at $T_{p,}$ decreases with increasing $T_{P.}$ The Curie temperature (T_C) also increases with increasing thickness, see Figure S7c. T_C and T_P for a specific LSMO film are almost equal, hence T_P in transport behavior can very well reflect the magnetic phase transition and metal-insulator transition (MIT) in LSMO. It can be concluded that the LSMO film with higher magnetization will have a lower MR effect.

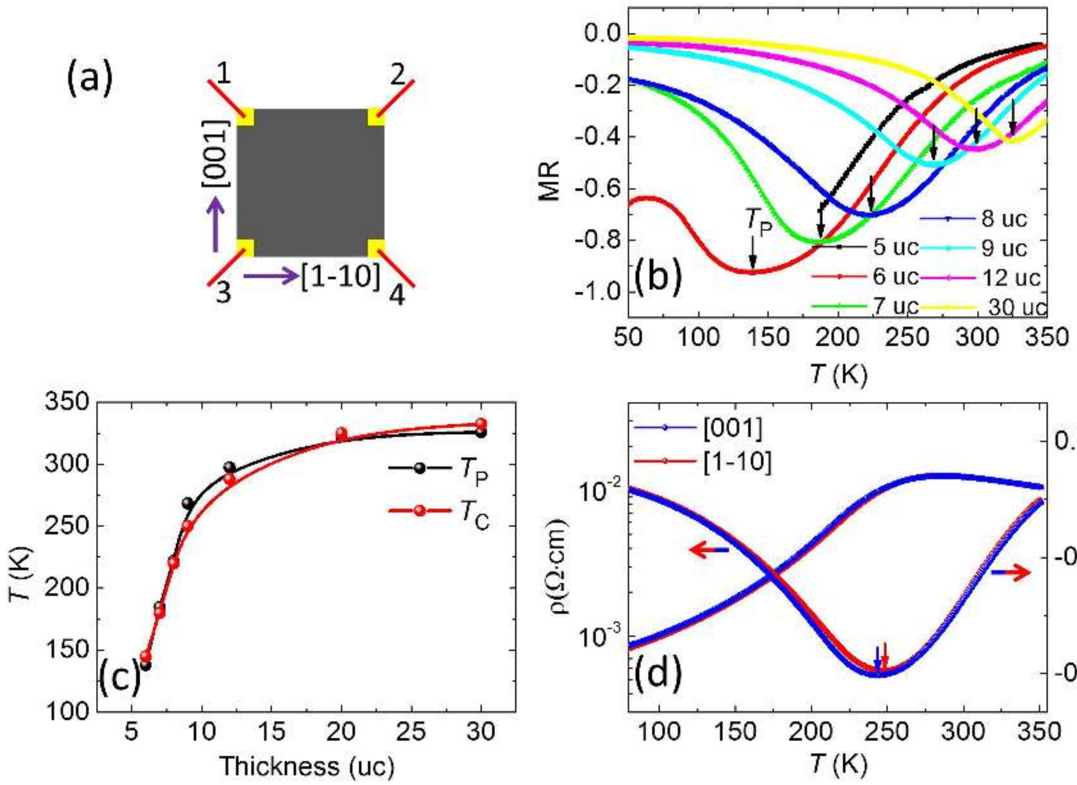

Figure S7 | Electrical characterization of LSMO thin films. a, Schematic of the resistivity measurement by van-der-Pauw geometry with four 0.5 mm × 0.5 mm gold electrodes at corners. The sample size is 5 mm x 5 mm. **b**, Temperature dependent $\mathrm{MR}_{[001]}$ (≡($\mathrm{R}_{[001]}$(9 T)-$\mathrm{R}_{[001]}$ (0 T))/$\mathrm{R}_{[001]}$ (0 T)) for LSMO films with different thicknesses under out of plane 9 T magnetic field. **c**, Thickness dependent T_C and T_P of LSMO films on NGO substrates. **d**, Temperature dependent resistivity and magnetoresistance MR=(R(B)-R(0))/R(0) along [001] and [1-10] for LSMO(6uc)/STO(9uc)/NGO sample. The MR was measured under out of plane 9 T magnetic field.

For a STO-buffered LSMO film, which behaves similar as a strain-dominated thick LSMO film, the transport anisotropy is very small as shown in Figure S7d. The STO buffered 6 uc LSMO film is more conductive than the non-buffered 6 uc LSMO film (data shown in Figure 4a in main text), consistent with the enhanced magnetism as mentioned in main text. The STO buffered 6 uc LSMO film exhibits very weak transport anisotropy. According to the temperature dependent MR curve, as shown in Figure S7d, the MR along [1-10] direction has a higher T_P, consistent with it's magnetic easy axis of [1-10].

7. Microscopic structural characterization of $La_{2/3}Sr_{1/3}MnO_3$/$NdGaO_3$ interface in (1-10) plane by STEM

The STEM images with zone axis along [1-10] were acquired to further clarify the octahedral tilt along ***b***-axis. Before showing STEM image, we would like to discuss the characteristics of orthorhombic distortion. The (1-10) and (001) projected NGO crystal structures are shown in Figure S8a and b respectively. For (1-10) plane, the out of phase rotation prevents us from precisely determining individual oxygen (O_1 and O_2) due to limited STEM spatial resolution (see Figure S8a), not like (001) plane (see Figure S8b). However, the orthorhombic distortion induces a zigzag A-sites (Nd) along ***a***-axis in (1-10) plane, as displayed in Figure S8a by the blue zigzag line. The ∠AAA angle (called φ and see Figure S8a) between three successive A-sites in same row in (1-10) plane for orthorhombic structure is correlated with tilts of the BO_6 octahedra [10]. For NGO, it is ~11.6^o [11]. With less orthorhombic distortion, the angle will decrease, e.g., in $SrRuO_3$, it is 5^o [12]. Going to cubic structure such as $SrTiO_3$, it becomes 0^o. The fact that all the A atoms in same column along [1-10] direction are projected to the exact same position allows as to accurately determine the A-site position and then extract the angle φ from STEM image. As a consequence of zigzag A-sites, the A site is close to its top and bottom oxygen alternately along ***a***-axis, as indicated by the blue-red ellipses in Figure S8a. These two features enable us to investigate the orthorhombic distortion from STEM image, besides only looking into the oxygen sites.

Now, let's turn to discuss the experimental results of (1-10) plane structure. The ABF-STEM image of (1-10) plane of 6 uc LSMO on NGO is shown in Figure S8c and the interfacial oxygen octahedral coupling (OOC) is observed. In NGO, due to out-of-phase rotation, the two neighbor oxygen O_1 and O_2 atoms merge to be one smearing and bigger atom as highlighted by blue ellipse in Figure S8c. The smearing of oxygen (O_1O_2) decays into LSMO layers. The smearing of oxygen at interface is comparable to that in bulk NGO, but smearing of the top O_1O_2 of first LSMO unit cell already becomes weaker than bulk NGO. The smearing of oxygen quickly decays and nearly disappears in 3rd LSMO unit cell. For example, in 3rd LSMO unit cell the single oxygen characteristics is clearly visible (see the red circles in Figure S8c), indicating very close of O_1 and O_2 and thus very small tilt of LSMO octahedra along ***b***-axis.

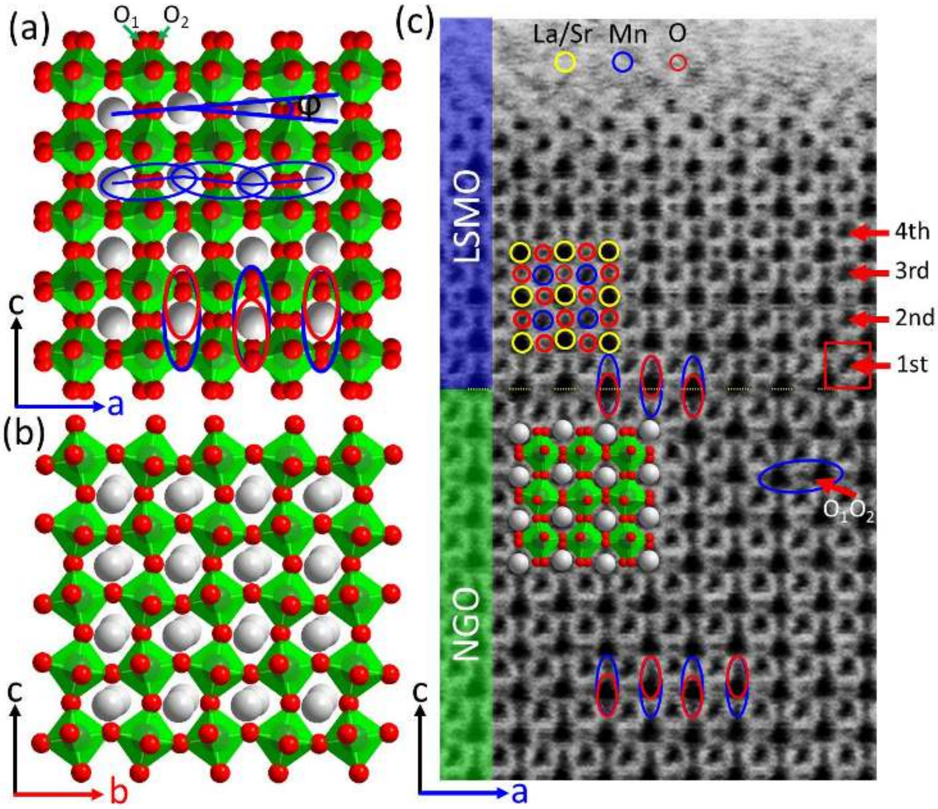

Figure S8 | Structure of LSMO/NGO interface. Projected structure model of NGO in (**a**) (1-10) and (**b**) (001) plane. **c**, ABF-STEM image of 6 uc LSMO on NGO (110) with zone axis along ***b***-axis. Inset shows the fitting of crystal structure into the STEM image.

Besides the smearing of oxygen, the zigzag A-sites along ***a***-axis and its alternately being close to top and bottom O_1O_2 are other evidences to demonstrate the octahedral distortion in (1-10) plane. The zigzag of A-sites in NGO can be seen and the crystal structure obtained from neutron scattering [11] can be fitted well with structure image from STEM (see Figure S8c). The red ellipse inside blue ellipse shows that the O_1O_2 slightly merges with A site and there is no clear boundary between O_1O_2 and A-site. This feature is also evident in interfacial LSMO layer indicated by the blue-red ellipses as well (see Figure S8c). The zigzag La/Sr at near interface region is indicated by the yellow circles. Therefore, the out-of-phase rotation along ***b***-axis in LSMO is directly evidenced by our ABF-STEM image from both the smearing of oxygen and zigzag A sites.

The $b^+a^-c^-$ at interface in contrast to $a^+b^-c^-$ in bulk film is illustrated by the relative octahedral tilt along two axis ***a*** and ***b***. Due to the out-of-phase rotation, we are not able to resolve O_1 and O_2 and thus measure the tilt angle directly, but there are two other evidences to confirm the $b^+a^-c^-$ of LSMO at near interface region. The NGO has $c^+a^-a^-$ rotation and the tilt of NGO octahedron along ***b***-axis is smaller than along ***a***-axis. The OOC effect along ***b***-axis then gives rise to smaller tilt in LSMO along this ***b***-axis. First, as shown in Figure S8c, the smearing of top oxygen in 1st LSMO unit cell is smaller than NGO, so the tilt of LSMO along ***b***-axis is expected to be smaller than NGO. In contrast, the tilt along ***a***-axis for LSMO is almost identical to NGO (see Figure 1b and 1e in main text). Therefore, a $b^+a^-c^-$ Glazer notation is suggested for near interface LSMO. The smearing of oxygen in 2nd and 3rd LSMO unit cell is very small, indicating small tilt, while along ***a***-axis, it is still relative big (see Figure 1e in main text). Therefore, there is an interfacial region where the tilt of LSMO is described by $b^+a^-c^-$.

Another evidence is from the ∠AAA (φ) angle in LSMO. As mentioned above, although we are not able to directly measure the tilt angle in (1-10) plane, but angle *a* and φ (see right panel of Figure S9a) which are connected to the octahedral tilt and well reflects the orthorhombic distortion can be precisely determined from STEM image [10]. As a result, we are able to quantify the orthorhombic distortion in (1-10) plane by measuring α and φ. Those angles were measured from annular dark field (ADF) image as shown in Figure S9a. The zigzag A-sites along ***a***-axis can be seen in NGO. To clearly visualize this zigzag pattern, we performed the gauss fitting of the image and obtained the individual A-site positions with which we are able to calculate the angles α and φ. An alternated sign of α (…+-+-+-…) will be present due to the zigzag pattern. The α for LSMO and NGO are shown in Figure S9b. Very clear oscillated α value is observed in NGO and first two LSMO layers. The α determined from STEM is ~ 5^o in NGO, well consistent with the value (~6^o) determined from neutron scattering [11], then decays into LSMO. Therefore, we are able to distinguish the out-of-phase along ***b***-axis ((1-10) plane) from in-phase along ***a***-axis ((001) plane) by determining the zigzag feature. The propagation of zigzag into LSMO also indicates the out-of-phase rotation nature of orthorhombic LSMO along ***b***-axis, consistent with XRD measurement [13].

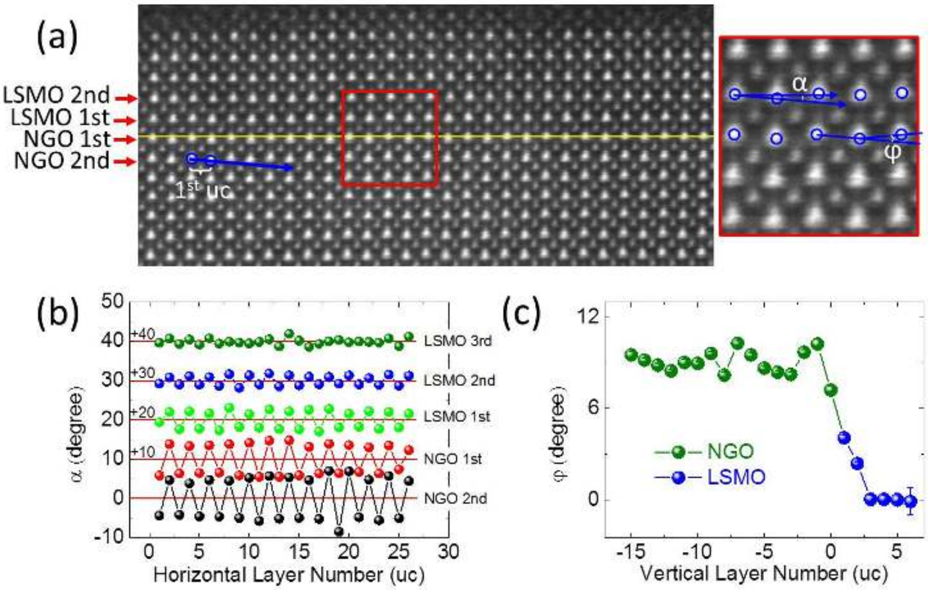

Figure S9 | Analysis of the orthorhombic distortion from STEM image. **a**, ADF image of LSMO(6 uc)/NGO. Right panel shows the zoom-in of selected square region in left pane and the definition of angle α and φ. Blue circles indicate the A-site atoms. **b**, The angle α as a function of horizontal unit cell number in same atom row. The first uc is defined by unit cell between third and fourth column and the first α in NGO 2nd layer is indicated by the white arrow. **c**, The φ as a function of layer number in vertical direction.

The decay nature of OOC is characterized by the decay of φ from interface into bulk LSMO. A statistical measurement of the φ is shown in Figure S9c. The φ is relatively big in first unit cell LSMO but is already smaller than that in NGO. From the 3rd unit cell, the φ is nearly decreased to 0^{o}. The decay of φ indicates the reduction of orthorhombic distortion from interface to bulk LSMO. The smaller φ in LSMO suggests a smaller octahedral tilt, consistent with the much smaller smearing of oxygen in LSMO as discuss above (see Figure S8c). We would like compare the distortion in (1-10) plane with the structure distortion in (001) plane shown in Figure 1e in main text. For (001) plane, the tilt angle along *a*-axis is still relative big in 3rd LSMO layer, but almost not visible in 3rd LSMO layer in (1-10) plane. Therefore, the tilt along *a*-axis is bigger than along *b*-axis. Similar analysis is done for first LSMO layer. At first

LSMO layer, along the *a*-axis the tilt angle is same with NGO, but along *b*-axis the tilt in LSMO is smaller than NGO. The decay of distortion shown in Figure S9c suggests a $b^+a^-c^-$ Grazer tilt at near interface region in LSMO.

Even assuming an extreme case that the tilt in first LSMO layer along *b*-axis was big enough to be identical to that in NGO, the $c^+a^-a^-$ nature of NGO would still give rise to $b^+a^-c^-$ tilt in LSMO at near interface region. In conclusion, the OOC effect is observed in (1-10) plane by STEM and our STEM results indicate the $b^+a^-c^-$ Glazer tilt in LSMO at the interface region.

8. Calculation of mean anisotropic energy constant from M-H curves

For uniaxial magnetic anisotropy, the magnetic anisotropy energy can be described by $E = K_u \mathrm{Cos}^2\varphi$ where φ is an in-plane angle relative to *a*-axis and K_u is the anisotropy energy constant. Here we neglect higher order terms. By measuring the field dependent magnetization M-H curve along the hard axis, to obtain H_K and M_S as shown in Figure S10, the K_u can be determined by formula $K_u = H_k \cdot M_S/2$ [14].

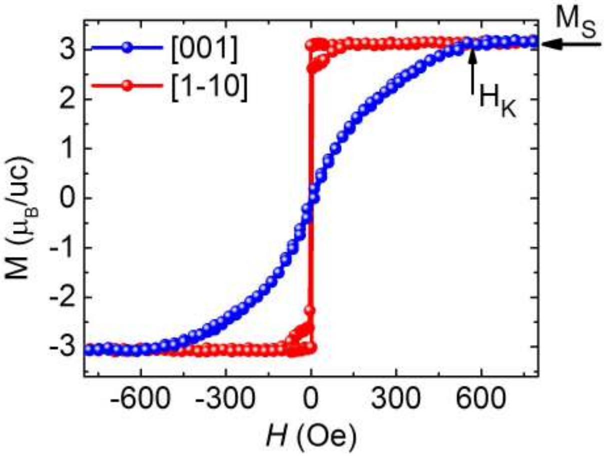

Figure S10 | M-H curves along two orthogonal directions taken at 100K for a 15 uc LSMO film on NGO (110) substrate. The arrows indicate the saturated magnetization M_S and switching field H_K where the magnetization starts to reach the saturated value M_S.

9. Density functional theory (DFT) based tight binding calculation of magnetic anisotropy energy

There are several sources of magnetic anisotropy, magnetocrystalline, shape, and exchange anisotropy. Since NGO and STO are not magnetic, we can exclude the exchange anisotropy with the substrate. Shape anisotropy is, on the other hand, only affecting the out-of-plane anisotropy, not the in-plane *a*- vs. *b*-axis anisotropy, which is at the focus of our study. From microscopic measurements of the Ga and Mn profiles, as shown in Figure 2d of main text, a chemically very sharp interface was concluded. Intermixing at the interface between LSMO and NGO is negligible. Although we cannot fully exclude very small amounts of inter-diffusion at the interface, the non-magnetic Ga would not contribute to the magnetic anisotropy. In manganites, the magnetic anisotropy strongly depends on the crystal structure and the variation of doping level does not switch the easy axis [15,16]. Furthermore, a substantial change of Mn valence at the interfaces due to non-polar STO buffer layer [17] could not be measured by EELS for our films [18]." The orbital polarization is also very small due to very small compressive strain and there is also no correlation between orbital polarization and magnetic anisotropy [18]. This leaves us with magnetocrystalline anisotropy, which is an intrinsic property of a ferromagnet. It depends on the crystal structure, but is independent of grain size and shape. The magnetic easy/hard axis of our LSMO ultrathin films on NGO is along a specific crystalline orientation such as [001] and [1-10] and, as we will show, can even be tuned by structural changes such as inserting an STO buffer layer or increasing thickness. Magnetocrystalline anisotropy can hence be expected to play the dominant role for the observed magnetic anisotropy.

The magnetocrystalline anisotropy originates from the spin-orbit coupling and can be qualitatively calculated by a tight-binding approach and perturbation analysis [19, 20]. To obtain a more realistic description for various materials, first principles density functional theory (DFT) calculations are desirable [21]. However, the magnetic anisotropy energy (MAE) (e.g. of LSMO ultrathin films in our study) is usually of the order of 1μeV/uc, which is much weaker than the exchange interaction of 1eV and is hence difficult to compute from DFT with sufficient numerical accuracy. A DFT based tight-binding Hamiltonian can overcome this problem and produce sub μeV precision [22].

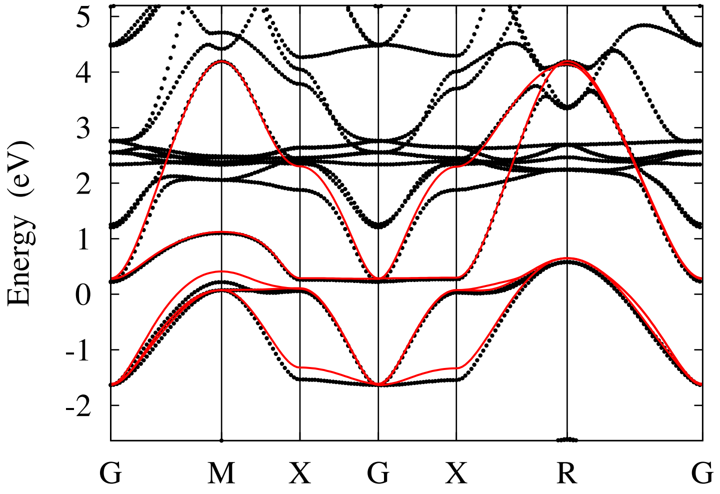

Figure S11 | DFT band structure (black) for 0.3% extensive stained LaMnO$_3$ and the tight binding band structure from Wannier projection (red). The small discrepancy arises from the entanglement of Mn e$_g$ bands with other bands.

We hence construct a DFT-based tight-binding Hamiltonian, $H(\vec{k}) + \left(\frac{\lambda}{2}\right)\sigma(\theta,\varphi) + \xi L \cdot S$, to calculate the MAE of LSMO ultrathin films. Here, the first term, $H(\vec{k})$, is the paramagnetic tight-binding Hamiltonian, constructed in the Wannier basis, which in turn was obtained from the projection of DFT-calculated Bloch waves of LSMO near the Fermi level. It has matrix elements $H_{\alpha\beta}(\vec{k}) = \sum_R t_{\alpha\beta}(\vec{R})\, e^{i\vec{K}\cdot\vec{R}}$ where $\vec{R}$ denotes lattice sites, α and β denote orbitals in Wannier basis with Mn d (d_{xy}, d_{yz}, d_{xz}, d_{z^2}, $d_{x^2-y^2}$) orbitals characters, $t_{\alpha\beta}(\vec{R})$ represents a hopping integral from orbital α at site 0 to orbital β at site $\vec{R}$, and k is the wave vector. For the DFT calculation we used the Wien2K package [23] with the PBE potential. The Wannier projection was performed with Wien2Wannier package [24], which employs Wannier90 for constructing maximally localized Wannier orbitals [25], for more details see Ref. [26]. We have performed the DFT calculation and Wannier function projection for both, cubic and 0.5% extensive strain. Figure S11 compares the Wannier bands with DFT for the latter case, where we get an anisotropy parameter (defined in the main text) A$_t$=0.6%.

The second term $\left(\frac{\lambda}{2}\right)\sigma(\theta,\varphi)$ describes an exchange splitting λ with magnetization along the direction (θ, φ), where σ(θ, φ) is the vector of Pauli matrices times a unit vector in the direction (θ, φ), so that a spin-up state in the (θ, φ)-direction has energy $+\frac{\lambda}{2}$ and a spin-down spin $-\frac{\lambda}{2}$. We employ $\lambda = 2$ eV which is the typical exchange splitting in manganites [27]. For the last term, the atomic spin orbit coupling of Mn *d* orbitals, we set $\xi = 0.05$ eV, a typical value for transition metals.

We diagonalize the Hamiltonian numerically and obtain the eigen-wavefunctions and eigen-energies $\varepsilon_i(k)$. Integrating over all k points in the first Brillouin zone, we obtain the total energy $E = \int_{BZ} \varepsilon_i(k)(\varepsilon_i - \varepsilon_F)dk$, where $f(\varepsilon_i - \varepsilon_F)$ is the Fermi-Dirac distribution at room temperature. The Fermi level ε_F is determined by the total number of d electrons per unit cell, i.e., $n = 3.67$ for $La_{2/3}Sr_{1/3}MnO_3$. Since the MAE of interest is of the order of 1 μeV/uc, we take advantage of the tight binding method and use a very fine k mesh (e.g. 160 × 160 × 160) to make sure that the total energy converges down to an accuracy of less than 10^{-3} μeV. Generally, the total energy, $E(\theta,\varphi)$, becomes a function of the magnetization orientation. In the absence of either magnetization ($\lambda = 0$) or spin-orbit coupling ($\xi = 0$), $E(\theta,\varphi)$ is constant. But for a ferromagnet ($\lambda \neq 0$) with spin orbit coupling ($\xi \neq 0$), it becomes energetically favorable if the magnetization points along a specific crystalline orientation, giving rise to magnetic anisotropy.

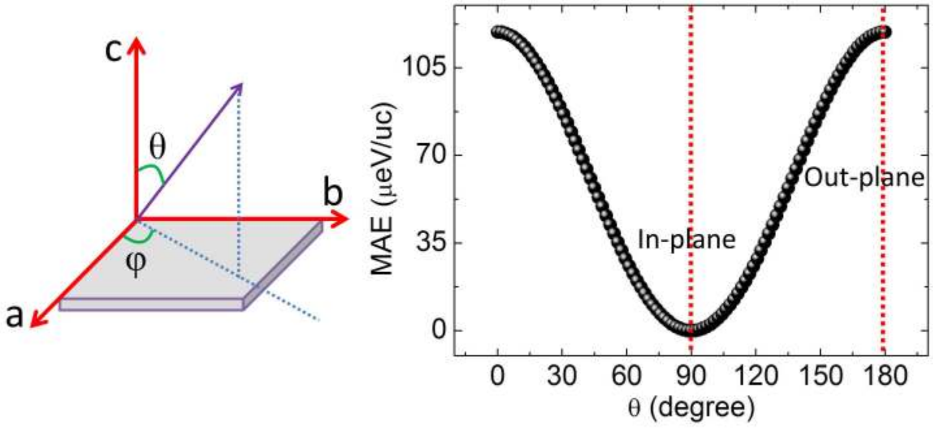

Figure S12 | DFT based tight binding calculation of MAE of single unit cell LSMO slab.

Figure S12 shows an example of the MAE as a function of θ for a free-standing monolayer LSMO film. The angle where MAE has its minimum defines the easy axis. In our case, we find that the easy axis lies in *ab* plane ($\theta = 90$ degrees). Due to the reduced symmetry, the out of plane MAE in thin films is strongly enhanced compared to that of the bulk [19-21]. The calculated energy scale of the out of plane MAE is ~0.1 meV/uc, quite consistent with the experimental values as mentioned above. Note that the shape anisotropy based on long-range dipole-dipole interactions can further modify this out of plane MAE [19]. The in-plane anisotropy (i.e., how the MAE depends on φ) is correlated to the asymmetric hopping factor A_t as described in main text. The in-plane anisotropic energy constant K is shown in Figure 5c of the main manuscript. It has an order of magnitude of 4 μeV/uc, consistent with experimental value.

10. Magnetic anisotropy of (001) LSMO films on cubic substrate

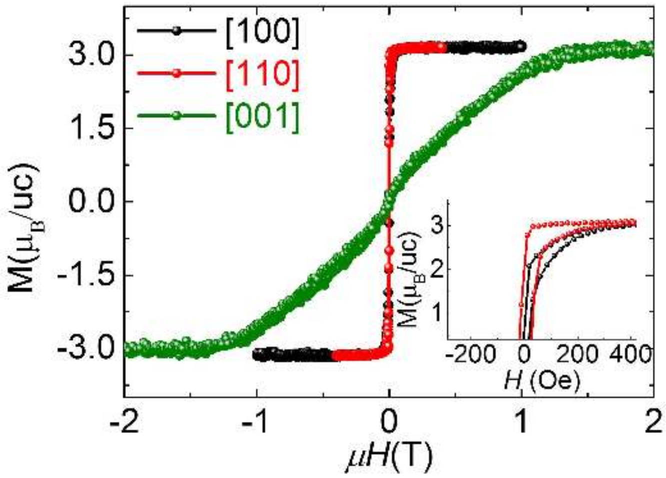

Figure S13 | Magnetic anisotropy of LSMO films on cubic STO (001) substrates at 100K. M-H curves of 30 uc LSMO film on STO (001) substrate along [100], [110] and [001] directions. Inset shows the zoom-in at low magnetic field region.

The (001) LSMO films grown on STO and $(LaAlO_3)_{0.3}(Sr_2AlTaO_6)_{0.7}$ (LSAT) both exhibit biaxial anisotropy with easy axis along $[110]_{pc}$ and $[1\text{-}10]_{pc}$ axis (pc represents pseudo-cubic index). The films were grown at same condition as films on NGO substrates. The LSMO films were coherently grown on these substrates as confirming by

RSM of $(024)_{pc}$, $(0\text{-}24)_{pc}$, $(204)_{pc}$, $(\text{-}204)_{pc}$ peaks, hence the in-plane structure is isotropic. Figure S13 shows the M-H curves for a 30 uc LSMO films on (001) STO substrate along different crystal orientations at 100 K.

The in-plane easy axis is determined to be $[110]_{pc}$ and $[1\text{-}10]_{pc}$. The in-plane magnetic anisotropy constant K ($\equiv H_K \cdot M_S/2$) is 5.5 μeV/uc. For out of plane direction, the H_K is 1.4 T and accordingly K is 0.13 meV/uc. Similar values are obtained when growing LSMO films on cubic (001) LSAT substrates.

11. Characterization of magnetic properties

The magnetization (M) was measured by using a QD-VSM. Since the NGO substrate is paramagnetic, a linear magnetic field (H) dependent magnetization contributes to each M-H curve. The magnetization of the LSMO films was acquired by subtracting the paramagnetic signal of the NGO substrate. To precisely measure the magnetization of LSMO ultrathin films such as 6 unit cell (uc), a driven model of VSM was used to achieve a measurement error of ~3×10^{-7} emu, which corresponds to 0.03 μ_B/uc for a 6 uc thick LSMO sample with an area of 5×5 mm^2. An example of the measurement of a 15 uc LSMO is shown in Figure S14.

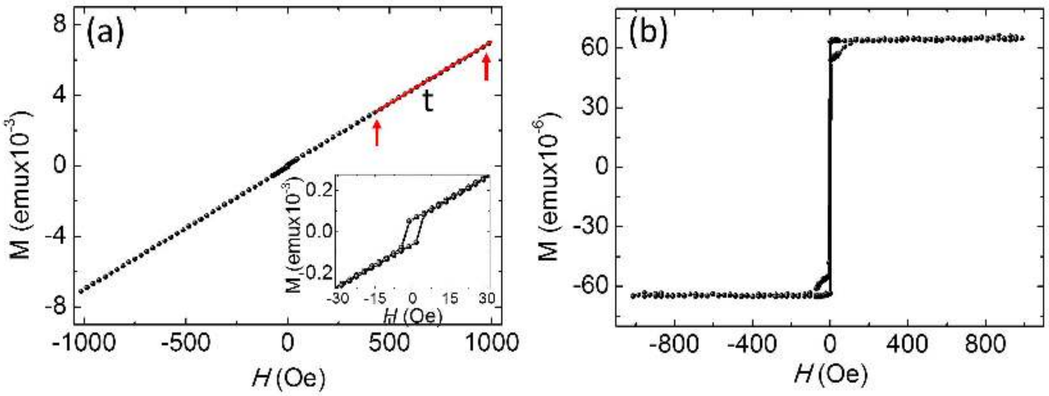

Figure S14 | Magnetic characterization of LSMO thin films. a, Raw measurement data of M-H curve of 15 uc LSMO film on NGO substrate at 100 K. Inset shows the zoom-in of low magnetic field region. **b**, Highly accurate M-H curve after subtracting the paramagnetic background signal of the NGO substrate.

The raw data in Figure S14a shows a hysteresis loop at low magnetic field, which originates from the ferromagnetic component of the LSMO film. By fitting the linear part at high field, a slope *t* is obtained and the NGO substrate signal can be removed from the overall signal by formula M(film) = M(total) - t × H. An accurate M-H curve can now be obtained for each LSMO film as can be seen in Figure S14b.

References:

[1] A.J. den Dekker, S. Van Aert, A. van den Bos and D. Van Dyck, Maximum likelihood estimation of structure parameters from high resolution electron microscopy images. Part I: A theoretical framework, *Ultramicroscopy* **104**, 83 (2005).

[2] S. Van Aert, A.J. den Dekker, A. van den Bos, D. Van Dyck and J.H. Chen, Maximum likelihood estimation of structure parameters from high resolution electron microscopy images. Part II: A practical example, *Ultramicroscopy* **104**, 107 (2005).

[3] G.T. Martinez, A. Rosenauer, A. De Backer, J. Verbeeck and S. Van Aert, Quantitative composition determination at the atomic level using model-based high-angle annular dark field scanning transmission electron microscopy, *Ultramicroscopy* **137**, 12 (2014).

[4] S. Macke & E. Goering, Magnetic reflectometry of heterostructures, *Journal of Physics: Condensed Matter*, **26**, 363201, (2014).

[5] S. Macke, A. Radi, J.E. Hamann-Borrero, A. Verna, M. Bluschke, S. Brück, E. Goering, R. Sutarto, F.Z. He, G. Cristiani, E. Wu, E. Benckiser, H.U. Habermeier, G. Logvenov, N. Gauquelin, G.A. Botton, A.P. Kajdos, S. Stemmer, G.A. Sawatzky, M.W. Haverkort, K. Keimer, and V. Hinkov, Element specific monolayer depth profiling, *Adv. Mater.* **26**, 6554 (2014).

[6] C. Chantler, Theoretical form-factor, attenuation and scattering tabulation for Z=1-92 from E=1-10 eV to E=0.4-1.0 MeV, *Journal of Physical and Chemical Reference Data* **24**, 71 (1995).

[7] website: www.remagx.org.

[8] C. Aruta, G. Ghiringhelli, V. Bisogni, L. Braicovich, N.B. Brookes, A. Tebano, and G. Balestrino, Orbital occupation, atomic moments, and magnetic ordering at interfaces of manganite thin films, *Physical Review B* **80**, 014431 (2009).

[9] O. Bierwagen, R. Pomraenke, S. Eilers & W.T. Masselink, Mobility and carrier density in materials with anisotropic conductivity revealed by van der Pauw measurements, *Phys. Rev. B* **70**, 165307 (2004).

[10] J.Y. Zhang, J. Hwang, S. Raghavan, & S. Stemmer, Symmetry lowering in extreme-electron-density perovskite quantum wells, *Phys. Rev. Lett.* **110**, 256401 (2013).

[11] L. Vasylechko, L. Akselrud, W. Morgenroth, U. Bismayer, A. Matkovskii, & D. Savytskii, The crystal structure of $NdGaO_3$ at 100 K and 293 K based on synchrotron data, *J. Alloys Compd.* **297**, 46 (2000).

[12] J.S. Gardner, G. Balakrishnan, D.McK. Paul, Neutron powder diffraction studies of Sr_2RuO_4 and $SrRuO_3$, Physica C 252, 303 (1995).

[13] A. Vailionis, H. Boschker, W. Siemons, E.P. Houwman, D.H.A. Blank, G. Rijnders, & G. Koster, Misfit strain accommodation in epitaxial ABO_3 perovskites: lattice rotations and lattice modulations, *Phys. Rev. B* **83** (6), 064101(2011).

[14] B.D. Cullity, Introduction to magnetic materials, Addison-Wesley, Reading, Mass., (1972).

[15] Y. Tokura (Ed.), Colossal Magnetoresistive Oxides, Gordon and Breach Science Publishers, The Netherlands, 2000, pp. 119-148.

[16] T.Z. Ward, J.D. Budai, Z. Gai, J.Z. Tischler, L. Yin, & J. Shen, Elastically driven anisotropic percolation in electronic phase-separated manganites, *Nature Phys.* **5**, 885 (2009).

[17] J.A. Mundy, Y. Hikita, T. Hidaka, T. Yajima, T. Higuchi, H.Y. Hwang, D.A. Muller, and L.F. Kourkoutis, *Nat. Commun.* **5**, 3464 (2014).

[18] Z. Liao et al, to be published.

[19] P. Bruno, Tight-binding approach to the orbital magnetic moment and magnetocrystalline anisotropy of transition-metal monolayers, *Phys. Rev. B* **39**, 865 (1989).

[20] S. Pick & H. Dreysse, Monolayer magnetic anisotropy: A systematical tight-binding study, *Phys. Rev. B* **46**, 5802 (1992).

[21] G.H. O. Daalderop, P.J. Kelly & M.F.H. Schuurmans, First-principles calculation of the magnetocrystalline anisotropy energy of iron, cobalt, and nickel, *Phys. Rev. B* **41**, 11919 (1990).

[22] N. Marzari, A.A. Mostofi, J.R. Yates, I. Souza & D. Vanderbilt, Maximally localized Wannier function s: Theory and applications, *Rev. Mod. Phys.* **84**, 1419 (2012).

[23] P. Blaha, K. Schwarz, G.K.H. Madsen, D. Kvasnicka & J. Luitz, WIEN2k, An augmented plane wave + local orbitals program for calculating crystal properties, Karlheinz Schwarz, Techn. Universitat, Wien, Austria, 2001.

[24] J. Kunes, R. Arita, P. Wissgott, A. Toschi, H. Ikeda & K. Held, Wien2wannier: From linearized augmented plane waves to maximally localized Wannier functions, *Comp. Phys. Comm.* **181**, 1888 (2010).

[25] A.A. Mostofi, J.R. Yates, Y.-S. Lee, I. Souza, D. Vanderbilt & N. Marzari, Wannier90: A tool for obtaining maximally-localized Wannier functions, *Comp. Phys. Comm.* **9**, 685 (2008).

[26] Z. Zhong, A. Toth & K. Held, Theory of spin-orbit coupling at $LaAlO_3$/$SrTiO_3$ interfaces and $SrTiO_3$ surfaces, *Phys. Rev. B* **87**, 161102 (2013).

[27] A. Yamasaki, M. Feldbacher, Y.-F. Yang, O.K. Andersen & K. Held, Pressure-induced metal-insulator transition in $LaMnO_3$ is not of Mott-Hubbard type, *Phys. Rev. Lett.* **96**, 166401 (2006).